KONAN UNIVERSITY

Random Walks in Relativistic Flow and Its Application to Gamma-Ray Bursts

(相対論的流体中でのランダムウォークと
そのガンマ線バーストへの応用)

A DISSERTATION SUBMITTED TO
THE GRADUATE SCHOOL OF KONAN UNIVERSITY
IN CANDIDACY FOR THE DEGREE OF
DOCTOR OF PHILOSOPHY

DEPARTMENT OF PHYSICS

BY

SANSHIRO SHIBATA

柴田　三四郎

KOBE, JAPAN
MARCH, 2015

ABSTRACT

The gamma-ray bursts (GRBs) are one of the most energetic phenomena in the universe. They radiate enormous energies of the order of 10^{51} ergs mainly in the form of gamma-rays with the short duration, typically of ~ 10 s. Although the radiation is thought to be originated from the ultra-relativistic jets with $\Gamma \gtrsim 100$, where Γ is the Lorentz factor of the jets, the radiation mechanism of gamma-rays is still under debate.

In this thesis, we investigate the random walk process in relativistic flow and construct an analytic expression for the effective optical depth in relativistic flow. Then, we apply the theory to the thermal photons radiated from relativistic jet which penetrates a stellar mantle of a massive star and results in the gamma-ray burst.

In the relativistic flow, photon trajectory is concentrated in the directions of the flow velocity due to relativistic beaming effect. We show that, in the pure scattering case, the number of scatterings is proportional to the size parameter $\xi \equiv L/l_0$ if the flow velocity $\beta \equiv v/c$ satisfies $\beta/\Gamma \gg \xi^{-1}$, while it is proportional to ξ^2 if $\beta/\Gamma \ll \xi^{-1}$ where L and l_0 are the size of the system in the observer frame and the mean free path in the comoving frame, respectively. We also examine the photon propagation in the scattering and absorptive medium. We find that, if the optical depth for absorption $\tau_{\rm a}$ is considerably smaller than the optical depth for scattering $\tau_{\rm s}$ ($\tau_{\rm a}/\tau_{\rm s} \ll 1$) and the flow velocity satisfies $\beta \gg \sqrt{2\tau_{\rm a}/\tau_{\rm s}}$, the effective optical depth is approximated by $\tau_* \simeq \tau_{\rm a}(1+\beta)/\beta$. Furthermore, we perform Monte Carlo simulations of radiative transfer and compare the results with the analytic expression for the number of scattering. The analytic expression is consistent with the results of the numerical simulations.

Therefore, we perform radiative transfer simulation for thermal radiation from GRB jet. The structure of the jet is derived by performing relativistic hydrodynamic simulation. The radiative transfer is calculated by postprocessing with a numerical code based on Monte Carlo method, which takes into account where the observed photons are produced in the jet and the cocoon. We find that the radiation from sub-relativistic cocoon partially contributes to the spectrum at lower energies, although the spectrum mainly consist of the radiation from ultra-relativistic jet. We compare our results to the Band function and find that the synthesized spectrum around the peak energy can be well fitted by the Band function, indicating that the thermal

emission may be observed as a non-thermal Band function.

TABLE OF CONTENTS

CHAPTER 1
INTRODUCTION

In this chapter, we summarize the observations of gamma-ray bursts. Firstly, we describe the history of the observations of gamma-ray burst from the discovery with the Vela satellite, and then we summarize the observational features of gamma-ray bursts.

1.1 Observational History of Gamma-Ray Bursts

Historically, GRBs were first discovered with the Vela satellite which was launched by the United State of America for the purpose of military use. In 1969, Vela observed the gamma-ray signals from outside of the Earth and the finding was reported in 1973 (Klebesadel et al. 1973). After that, BATSE, which was a gamma-ray detector equipped on the Compton Gamma-ray Observatory launched also by U.S.A, detected a lot of events and found that the directions of GRBs are almost isotropically distributed in the universe. Figure 1.1 shows the directions of 2704 GRBs.

The uniform distribution of GRBs indicates that they are originated from old stars such as neutron stars in the Galactic halo or other galaxies with the cosmological distances from our galaxy. This is because most of the luminous main sequence stars in our galaxy locate in the disk and the ditribution of nearby galaxies have some structures in the sky.

The problem whether the origin of GRBs is Galactic or cosmological distant galaxies was not clarified until the late 1990s. In 1997, Italian-Dutch X-ray satellite Beppo-SAX discovered the X-ray emission following the prompt gamma-ray emission of GRB 970228 (Costa et al. 1997). This emission could be detected even several days after the gamma-ray trigger and called the afterglow. After the discovery of the afterglow, follow-up observations by ground-based optical telescopes are performed and the afterglow in optical band was also found (van Paradijs et al. 1997). The observations in the optical afterglow enabled the astronomers to identify a host galaxy of GRBs and it was confirmed that the GRBs occurs in the galaxies at the cosmological distance from the Milky Way (e.g., Metzger et al. 1997; Kulkarni et al. 1998; Djorgovski et al. 1998).

On the other hand, it had been suggested that, if the GRBs have a cosmological

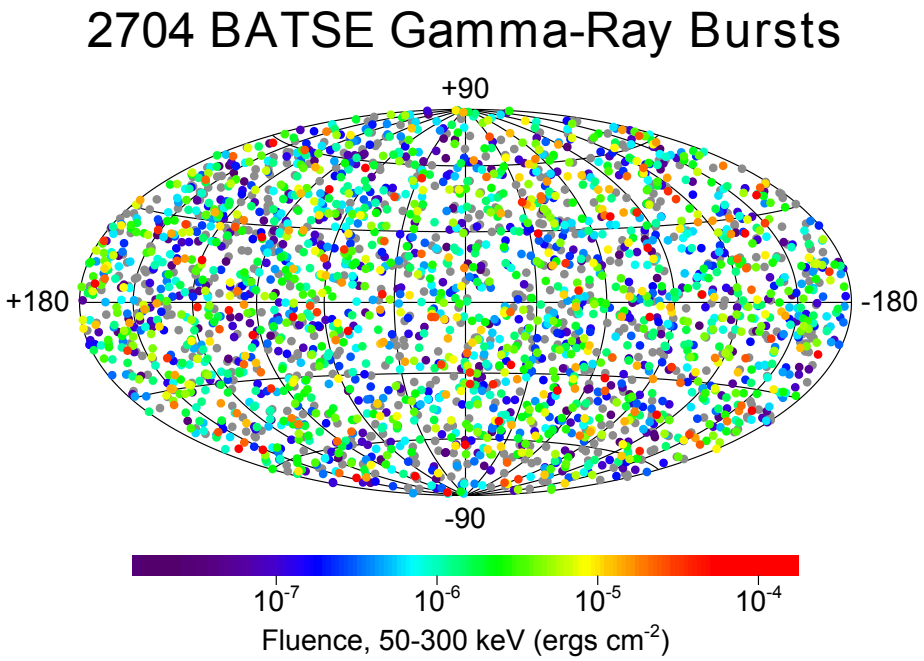

Figure 1.1 Directions of 2704 GRBs observed by BATSE. (http://gammaray.nsstc.nasa.gov/batse/grb/skymap/)

origin, the non-thermal spectrum of gamma-ray emission was thought to be inconsistent with very high opacity for $\gamma\gamma$ absorption at the source, called "compactness problem" (Ruderman 1975). Nowadays, it is known that the compactness problem is avoidable if the gamma-rays are emitted from ultra-relativistic outflows with $\Gamma \gtrsim 100$ where Γ is Lorentz factor of the outflow (see Section 1.3.1).

Furthermore, the cosmological distance of the origin of GRBs indicates that enormous energies are released as the gamma-ray emissions. Assuming that the gamma-rays are radiated isotropically, the released energies can be estimated as high as $E_{\gamma,\mathrm{iso}} \sim 10^{53}$ ergs for the typical GRB and $E_{\gamma,\mathrm{iso}} \sim 10^{54}$ ergs for the most powerful bursts. This extremely large energy is comparable to the rest mass energy of the Sun, $M_\odot c^2 \sim 2 \times 10^{54}$ ergs. However, in 1999, Harrison et al. (1999) found an achromatic break in the light curve of the optical afterglow of GRB 990510 (Figure 1.2) and the break indicates the existence of the edge of the outflow, which means that the outflow is not isotropic but has a shape of jet with a finite opening angle of $\theta \sim 5°$. Since a half opening angle θ_{jet} corresponds to a solid angle of $\Omega = 2\pi(1 - \cos(\theta_{\mathrm{jet}})$, the collimation-corrected released energies can be reduced to $E_\gamma = (1 - \cos\theta_{\mathrm{jet}})E_{\gamma,\mathrm{iso}}$ and

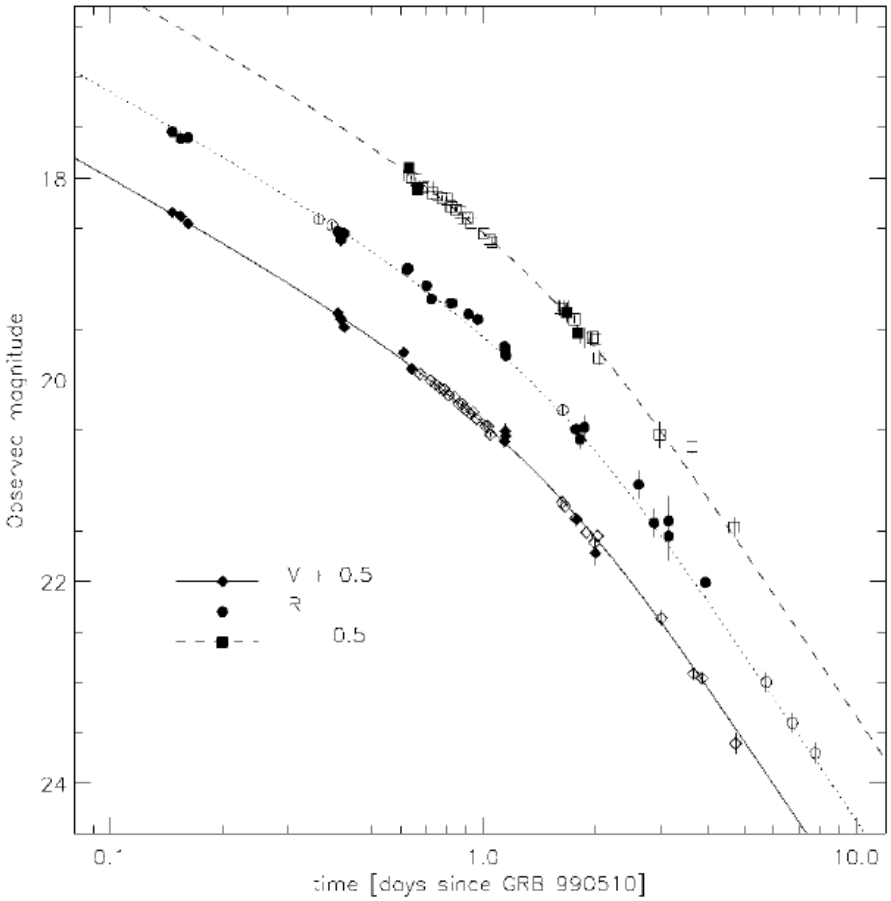

Figure 1.2 Optical light curve of GRB 990510. A break at $t \sim 1$ days indicate that the outflow has a shape of jet with a finite opening angle. (Harrison et al. 1999)

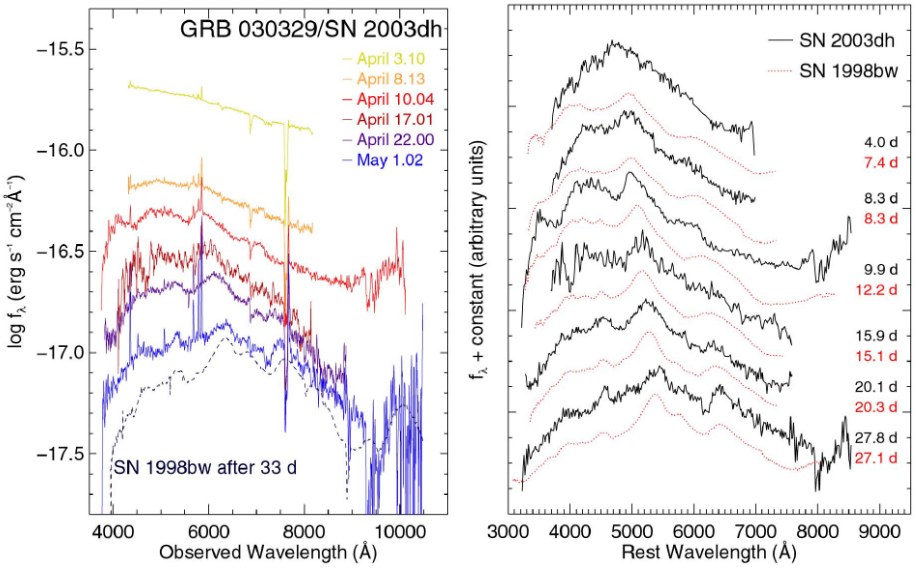

Figure 1.3 Optical spectra of GRB 030329/SN 2003dh (Hjorth et al. 2003). The left panel shows the evolution of the spectra and the right panel shows comparisons with the spectra of SN 1998bw which is also GRB associated supernova.

Harrison et al. (1999) estimated the released energy of GRB 990510 as $E_\gamma \sim 10^{51}$ ergs which is comparable to the kinetic energy of supernovae.

Although it had been known that GRBs occur in galaxies at cosmological distance, the specific sources of GRBs were not clarified yet. However, in 1998, Beppo-SAX observed the afterglow of GRB 980425 and soon after a supernova, named SN 1998bw, was discovered at the same position of GRB 980425 (Galama et al. 1998). From the coincidense, a connection between GRB and SN was suggested. SN 1998bw was classified into Type Ic supernova but was more luminous than ordinal Type Ic supernovae and have much broader spectral lines which indicates a very energetic explosion. Iwamoto et al. (1998) constructed a model reproducing optical observations of SN 1998bw and estimated its kinetic energy as $E_{\rm kin} \sim 10^{52}$ erg which is one order of magnitude higher than the kinetic energy of ordinal supernovae. Such unusually energetic explosions have been called as hypernova. In addition, in 2003, high energy transient explorer HETE-II detected GRB 030329 and soon follow-up observations of the optical afterglow was performed (Hjorth et al. 2003). As a result, the redshift of GRB 030329 was estimated as $z = 0.17$ and, surprisingly, it was found that the spectrum of the optical afterglow of GRB 030329 evolved to the spectrum of a broad

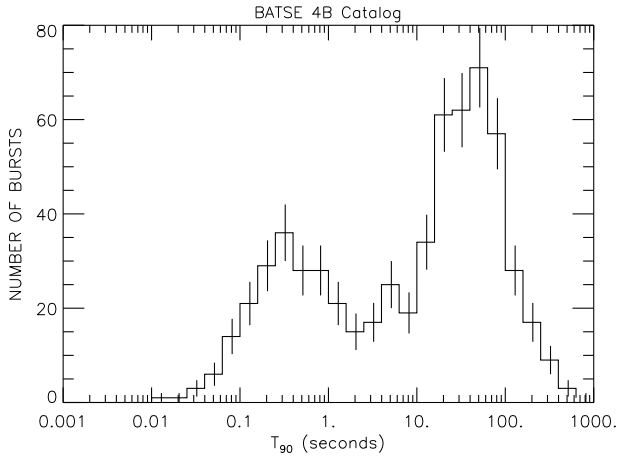

Figure 1.4 Distribution of the duration of gamma-ray emissions observed by BATSE. T_{90} is a time duration in which 90% of the total energies are radiated. (Paciesas et al. 1999, http://gammaray.nsstc.nasa.gov/batse/grb/duration/)

line type Ic supernova SN 2003dh which is very similar to the optical spectrum of SN 1998bw. Therefore, it was concluded that a GRB and broad line Type Ic SN have a same origin, which is the core collapse of massive stars.

However, it should be noted that there are two types of GRBs distinguished by their duration of the gamma-ray emissions. Figure 1.4 shows a distribution of the duration of gamma-ray emissions observed by BATSE, which has double peakes at 0.1s and 10s. This indicates the existence of two populations. GRBs with duration longer than 2s is called long gamma-ray burst (long GRB) and GRBs with duration shorter than 2s is called short gamma-ray burst (short GRB). All of the GRBs accompanying SNe belong to long GRBs. It is widely believed that although long GRBs are related to the core collapse of massive stars, short GRBs have another origins. One of the possible candidates for the origin of short GRBs is merger of binary neutron stars. Fox et al. (2005) observed the afterglow of GRB 050709, which is a short GRB, and ruled out the existence of associated supernova component.

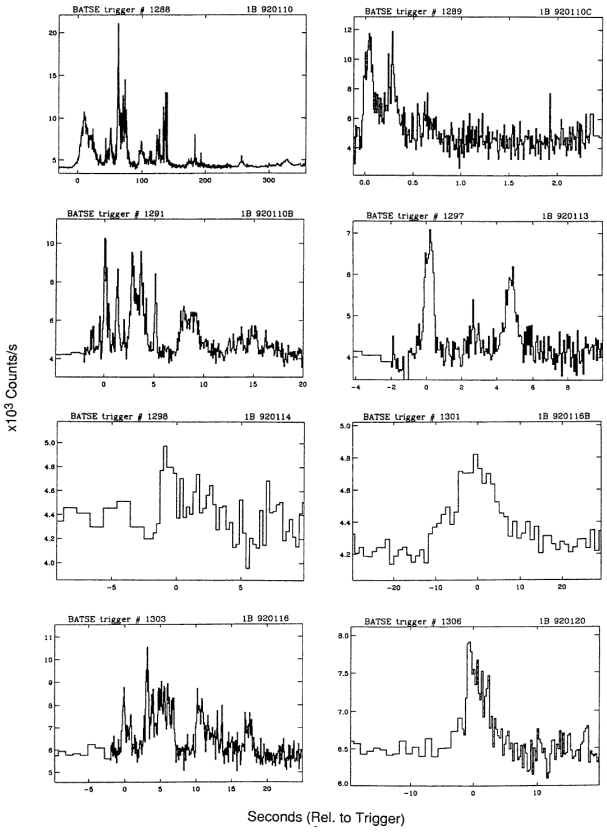

Figure 1.5 Light curves of GRBs observed by BATSE. (Fishman & Meegan 1995)

1.2 Observational Properties of GRB Emissions

1.2.1 Prompt Emission

As mentioned in the previous section, there are two kinds of radiations from GRBs: one is the initial prompt emission which is mainly in gamma-ray energy band and the another is less energetic afterglow observed in X-ray, UV, optical, infrared, and radio band. Here, we briefly describe the fundamental properties of the prompt emission.

Light curves of the prompt emission show strong time variabilities. Basically, they rise very fast and then decay exponentially, and many bursts have some peaks in their light curves. Figure (1.5) shows light curves of GRBs observed by BATSE. Since the time scales of the variablities are very short, it can be expected that the size of the origin of GRB is correspondinly small.

The energy spectrum of prompt emission has a non-thermal shape with a peak

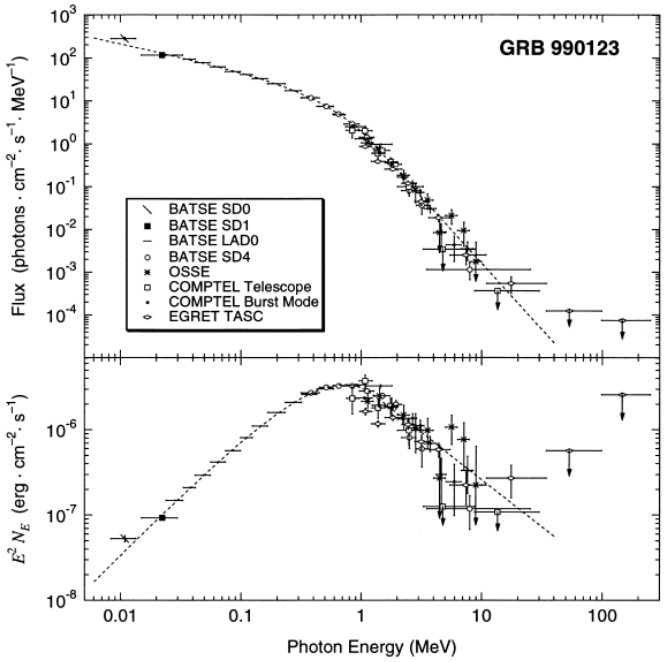

Figure 1.6 Time averaged spectrum of GRB 990123. Fitting paramters are $E_{\rm peak} = 720$ keV, $\alpha = -0.6$, and $\beta = -3.11$. (Briggs et al. 1999)

energy typically of ~ 100 keV and it can be well fitted by an empirical function, called Band function (Band et al. 1993). The Band function has two power-law indices at high and low energy side. These are connected smoothly at a break energy $E_{\rm b}$ as follows,

$$f_{\rm BAND}(E) = A \times \begin{cases} \left(\frac{E}{100}\right)^{\alpha} \exp\left[-\frac{E(2+\alpha)}{E_{\rm peak}}\right] & \text{for } E < E_{\rm b}, \\ \left[\frac{(\alpha-\beta)E_{\rm peak}}{100(2+\alpha)}\right]^{\alpha-\beta} \exp(\beta-\alpha)\left(\frac{E}{100}\right)^{\beta} & \text{for } E \geq E_{\rm b}, \end{cases} \tag{1.1}$$

where $f_{\rm BAND}$ is a function of photon number and break energy $E_{\rm b}$ is related to $E_{\rm peak}$ as

$$E_{\rm b} = (\alpha - \beta)\frac{E_{\rm peak}}{2+\alpha}. \tag{1.2}$$

This function consists of with four parameters: its absolute value A, low energy photon index α, high energy photon index β, and peak energy in the spectral energy distrubution $E_{\rm peak}$. Figure 1.6 shows the energy spectrum of GRB 990123 observed by BATSE. The fitted Band function is also shown in Figure 1.6. Figure 1.7 shows the

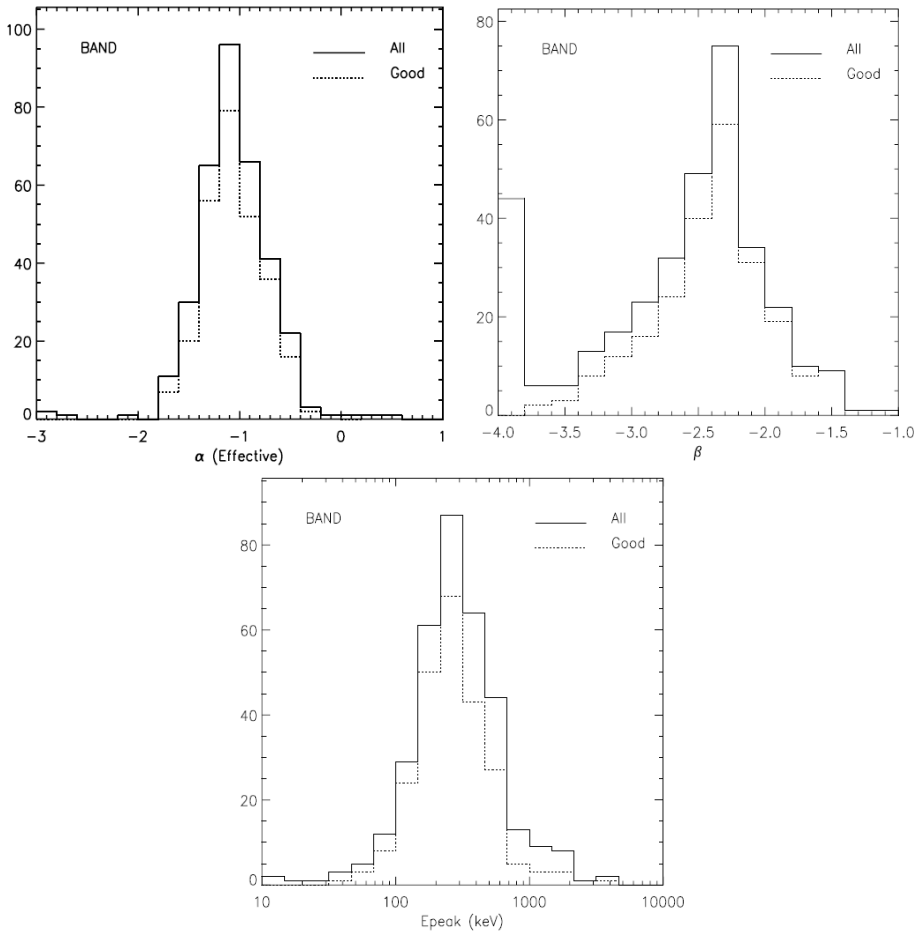

Figure 1.7 The statics of the parameters by which the spectra of GRBs observed by BATSE were fitted. (Kaneko et al. 2006)

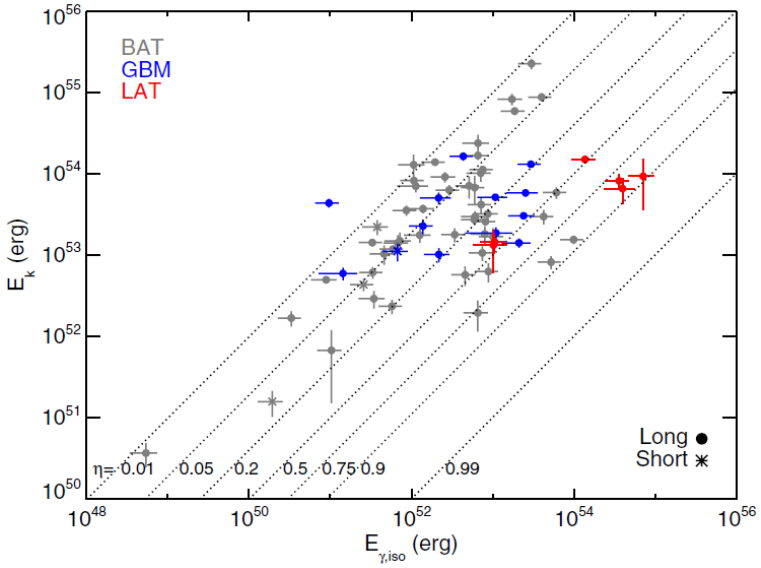

Figure 1.8 Distribution of the observed gamma-ray energy $E_{\gamma,\mathrm{iso}}$ and the kinetic energy of the jet estimated by the afterglow. The gamma-ray energies are assumed to be isotropic. Dotted lines indicate contours that the radiative efficiency of gamma-ray is constant. (Racusin et al. 2011)

distributions of the fitting parameters for GRBs observed by BATSE (Kaneko et al. 2006). The typical values of α, β, and E_{peak} are -1, -2.5, and 300 keV, respectively.

Figure 1.8 shows the distribution of the observed gamma-ray energy $E_{\gamma,\mathrm{iso}}$ and the kinetic energy of the jet estimated by the afterglow (Racusin et al. 2011). Here, the gamma-ray energies are assumed to be isotropic. Dotted lines indicate contours that the radiative efficiency of gamma-ray emission is constant. The radiative efficency is defined as

$$\eta = \frac{E_{\gamma,\mathrm{iso}}}{E_{\gamma,\mathrm{iso}} + E_{\mathrm{kin}}}, \tag{1.3}$$

where $E_{\gamma,\mathrm{iso}}$ and E_{kin} are the isotropic gamma-ray energy and the kinetic energy of the jet, respectively. Although some GRBs show relatively small efficiencies like $\eta \sim 1\%$, GRBs with $\eta > 50\%$ also exist.

1.2.2 Afterglow

As mentioned in Sec 1.1, the prompt gamma-ray emissions are followd by less energetic afterglows, which are observed in X-ray, UV, optical, infrared, and radio band.

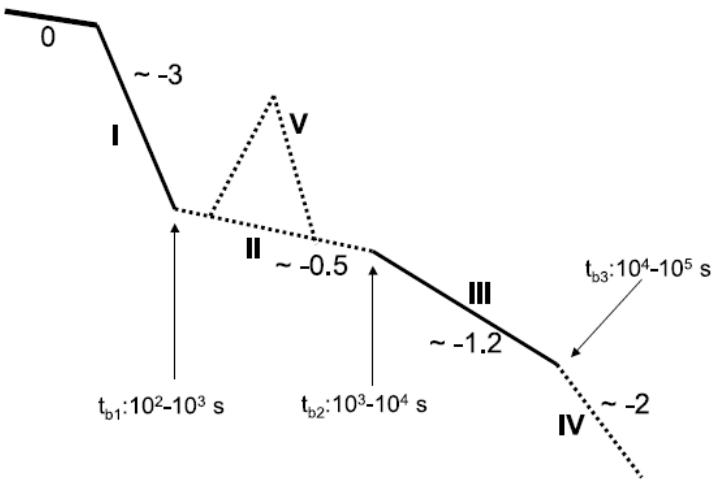

Figure 1.9 A schematic picture of X-ray afterglow. (Zhang et al. 2006)

Basically, the lightcurve of the afterglow is a combination of power-laws with different indices and sometimes a flare occurs. In this section, we briefly describe the propeties of X-ray afterglow.

We express the energy flux of X-ray afterglow as

$$F(\nu, t) \propto t^{-a}\nu^{-b}. \tag{1.4}$$

The light curve of X-ray afterglow can be divided into 5 phases: (I) initial steep decay phase at around 300 s $< t_1 <$ 500 s. The temporal index a_1 is $3 < a_1 < 5$ and the specral index b_1 is $1 < b_1 < 2$. (II) relatively flat decay phase at 10^3 s $< t_2 < 10^4$ s which was found by Swift satellite, and the temporal and spectral indeces are $0.2 < a_2 < 0.8$ and $0.7 < b_2 < 1.2$, respectively. (III) Normal decay phase at $t_3 < 10^5$ s. The temporal and spectral indeces are $1.1 < a_3 < 1.7$ and $0.7 < b_3 < 1.2$, respectively. (IV) relatively steep decay phase at $t_4 > 10^5$ s of the jet break. The temporal and spectral indices are $2 < a_3 < 3$ and $0.7 < b_3 < 1.2$, respectively. (V) X-ray flares sometimes occur at a period from immediately after the prompt emission to 10^5 s. The energy of the flare ranges from a few % to several tens % of the energy of prompt emission. The light curve of the X-ray flare behaves as $(t - t_0)^{\pm\alpha_{\rm fl}}$ where t_0 and $\alpha_{\rm fl}$ are the reference time and the temporal index of $3 \lesssim \alpha_{\rm fl} \lesssim 6$, respectively. Figure 1.9 shows a schematic picture of the light curve of X-ray afterglow.

1.3 Theoretical Framework of Gamma-ray Bursts

1.3.1 Compactness Problem

Since the energy spectrum of the prompt emission is non-thermal, the radiating region is thought to be optically thin. This constrains the motion of the matter which emits the gamma-ray photons (e.g., Lithwick & Sari 2001).

We consider a typical burst with energy flux F. If it occurs at a distance D from us, its luminosity is estimated as

$$L = 4\pi D^2 F = 4 \times 10^{51} \left(\frac{D}{6000 \text{ Mpc}} \right)^2 \left(\frac{F}{10^{-6} \text{ erg/cm}^2\text{/s}} \right) \text{ erg/s}, \tag{1.5}$$

where we assume isotorpic radiation and, since the observed time scale of the variability is as small as $\delta T \sim 10$ ms, the size of the origin of the burst R_i can be constrained as $R_\mathrm{i} < c\delta T \sim 3000$ km.

The observed spectrum consists of a lot of high energy photons. The high energy photon (with energy E_1) interact with a low energy photon (with E_2) and creates electron positron pair if the condition $E_1 E_2 > (m_\mathrm{e} c^2)^2$ is satisfied. The number of radiated photons is estimated as $N_\gamma \sim 4\pi D^2 F \delta T / \bar{E_\gamma}$, where $\bar{E_\gamma}$ is an typical photon energy. If we denote the fraction of photons which can cause pair production by f_p, the optical depth for pair production at the source is calculated by $\tau_{\gamma\gamma} \sim f_\mathrm{p} N_\gamma \sigma_\mathrm{T} / 4\pi R_\mathrm{i}^2$, where σ_T is the Thomson cross section. Substituting N_γ into the above equation, $\tau_{\gamma\gamma}$ can be estimated as

$$\tau_{\gamma\gamma} \sim \frac{f_\mathrm{p} \sigma_\mathrm{T} F D^2 \delta T}{\bar{E_\gamma} R_\mathrm{i}^2} \tag{1.6}$$

or

$$\tau_{\gamma\gamma} \sim 10^{15} f_\mathrm{p} \left(\frac{F}{10^{-6} \text{ erg/cm}^2} \right) \left(\frac{D}{6000 \text{ Mpc}} \right)^2 \left(\frac{\delta T}{10 \text{ ms}} \right)^{-1}. \tag{1.7}$$

Here, we assumed $R_\mathrm{i} \sim c\delta T$. This optical depth is extremely large and inconsistent with the observed non-thermal spectrum (1.2.1). This is called the compactness problem (e.g., Piran 2004; Lithwick & Sari 2001). The compactness problem can be resolved if one consider ultla-relativistic motion of the emitting material toward the observer.

Firstly, if the emitting matter moves with the Lorentz factor Γ, a photon observed with the energy of E_obs in laboratory frame has the energy of $E' \simeq E_\mathrm{obs}/\Gamma$ in

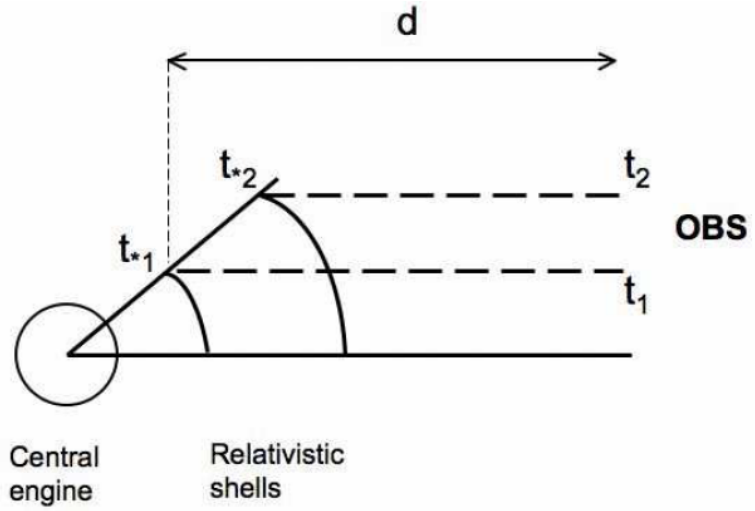

Figure 1.10 Radiations from front and back sides of a relativistically moving shell with finite width. (Mészáros 2006)

the matter comoving frame. Thus, the condition for the pair prodcution $E'_1 E'_2 > (m_e c^2)^2$ in the comoving frame is replaced by the condition in laboratory frame $E_1 > \Gamma^2 (m_e c^2)^2 / E_2 \propto \Gamma^2$ and f_p in laboratory frame decreases correspondingly because $f_p \propto \int_{E_1} N(E) dE \propto E_1^{\beta+1} \propto \Gamma^{2(\beta+1)}$. Here, β is the high energy photon index $N(E)dE \propto E^\beta dE$.

Secondly, if the matter has a relativistic velocity, the estimation of the size from time variability $R_i \sim c\delta T$ is replaced by $R_i \sim 2\Gamma^2 c\delta T$. This can be understood by considering radiations from front and back sides of a relativistically moving shell with finite width. Let δT_* and δT are the arrival time delay of two radiations in the comoving and laboratory frame, respectively. Then these two values are related by the following relation

$$\delta T = \delta T_* (1 - \beta\mu) \simeq \delta T_* (1/2\Gamma^2 + \theta^2/2) \simeq R_i/(2\Gamma^2 c)(1 + \Gamma^2\theta^2) \simeq R_i/(2\Gamma^2 c). \quad (1.8)$$

Here, we assumed that the emitting regions are inside light cone, that is $\theta \ll \Gamma^{-1}$, and $\Gamma \gg 1$. Hence, the size of the region is estimated by $R_i \sim 2\Gamma^2 c\delta T$ instead of $R_i \sim c\delta T$.

Therefore, the optical depth for the pair production is reduced to

$$\tau_{\gamma\gamma} \sim \frac{f_{\rm p}}{\Gamma^{-2(\beta+1)}} \frac{\sigma_{\rm T} F D^2 \delta T}{\bar{E}_\gamma R_{\rm i}^2} \tag{1.9}$$

or

$$\tau_{\gamma\gamma} \sim \frac{10^{15}}{\Gamma^{-2\beta+2}} f_{\rm p} \left(\frac{F}{10^{-6}\ {\rm erg/cm^2}}\right) \left(\frac{D}{6000\ {\rm Mpc}}\right)^2 \left(\frac{\delta T}{10\ {\rm ms}}\right)^2. \tag{1.10}$$

Substituting the observed typical value of $\beta = -2.5$ (1.2.1), if the matter moves toward the observer with a Lorentz factor $\Gamma > 10^{15/(-2\beta+2)} \sim 100$, $\tau_{\gamma\gamma}$ decreases to $\tau_{\gamma\gamma} \lesssim 1$ and the compactness problem can be resolved.

1.3.2 Relativistic Fireball Model

Thermodynamical Evolution of Fireball

GRBs are thought to be a phenomena that an enormous energy $E \sim 10^{51}$ erg is released from an small region $R_{\rm i} \lesssim 1000$ km. In such a system, matter is thought to be hot, called fireball, and the thermodynamical evolution of the fireball have been studied by many authors (e.g., Paczynski 1986; Goodman 1986; Meszaros et al. 1993; Piran et al. 1993) Here, for simplicity, we treat the fireball as a steady spherically symmetric wind and discuss its thermodynamical evolution. The equations of mass and energy conservation in such wind is written as (e.g., Blandford & McKee 1976)

$$4\pi r^2 \rho \Gamma c = \dot{M} \tag{1.11}$$

$$4\pi r^2 \left(\rho c^2 + \frac{4}{3} e_{\rm int}\right) \Gamma^2 c = \dot{E} \sim L_{\rm iso}, \tag{1.12}$$

where Γ, ρ, and $e_{\rm int}$ are the Lorentz factor, density, and internal energy density, respectively. We assumed that the velocity is almost speed of light $v \sim c$ and used the equation of state for relativistic particles $p = e_{\rm int}/3$, where p is a pressure. $\dot{M}$ and $\dot{E}$ are the released mass and energy per unit time. From Equation (1.11), we obtain constant $r^2\rho\Gamma$ which leads to a relation $\rho \propto \Gamma r^2$. Since the matter should be initially radiation dominated, which means $e_{\rm int} \sim aT^4 \gg \rho c^2$, $r^2 T^4 \Gamma$ is constant. Since the adiabatic index of radiation dominated matter is $\gamma_{\rm a} = 4/3$, the temperature relates with the density as $T \propto \rho^{\gamma-1} = \rho^{1/3}$ and the combination leads to $r^{-2/3}\Gamma^{2/3} \propto$ const, thus $\Gamma \propto r$. The temperature and the density decreases as $T \propto r^{-1}$ and $\rho \propto r^{-3}$.

However, once the matter expands and cools, it becomes matter dominated, $e_{\rm int} \ll \rho c^2$ and, from Equation (1.11) and(1.12), the Lorentz factor reaches its maximum value $\Gamma_{\rm max} \sim \eta \equiv L_{\rm iso}/\dot{M}c^2$ and remains constant

$$\Gamma(r) \sim \begin{cases} r/r_0, & \text{for } r < r_{\rm s} \\ \eta & \text{for } r \geq r_{\rm s}, \end{cases} \tag{1.13}$$

where $r_{\rm s} \sim r_0\eta$ is a saturation radius above which the Lorentz factor is constant. Above the saturation radius ($r > r_{\rm s}$), the temperature and density decreases as $T \propto \rho^{1/3} \propto r^{-2/3}$, that is

$$\frac{T}{T_0} = \left(\frac{\rho}{\rho_0}\right)^{1/3} \simeq \begin{cases} (r_0/r) & \text{for } r < r_{\rm s}, \\ \eta^{-1/3}(r_0/r)^{2/3} & \text{for } r > r_{\rm s} \end{cases} \tag{1.14}$$

where T_0 and ρ_0 are the initial temperature and density, respectively.

From $4\pi r_0^2 caT_0^4 \simeq L_{\rm iso}$ and $4\pi r_0^2 \rho_0 \Gamma_0 c = \dot{M} \sim L_{\rm iso}/\eta c^2$, the initial temperature and the density are estimated as

$$kT_0 \simeq 1.2 \left(\frac{L_{\rm iso}}{10^{52}\ {\rm erg/s}}\right)^{1/4} \left(\frac{r_0}{10^7\ {\rm cm}}\right)^{-1/2}\ {\rm MeV} \tag{1.15}$$

$$\rho_0 \simeq 10^3 \left(\frac{L_{\rm iso}}{10^{52}\ {\rm erg/s}}\right) \left(\frac{r_0}{10^7\ {\rm cm}}\right)^{-2} \left(\frac{\eta}{300}\right)^{-1}\ {\rm g/cm^3}. \tag{1.16}$$

Photospheric Emission from Fireball

The initial temperature of the fireball is as high as $kT_0 \sim 1$ MeV. In such condition, the production of a large number of electron-position pairs are expected and the scatterings by these electron-positron pairs are thought to be a dominant opacity source. However, if the temperature of the matter decreases as low as $kT \sim 20$ keV, the contributions from the pairs will be nagligible and the scatterings by the electrons which is accompanied with the baryons becomes dominant (Paczynski 1986). The transition radius $r_{\rm p}$ above which $e^{\pm}$ pairs are negligible is

$$r_{\rm p} \simeq 6 \times 10^8 \left(\frac{L_{\rm iso}}{10^{52}\ {\rm erg/s}}\right)^{1/4} \left(\frac{r_0}{10^7\ {\rm cm}}\right)^{1/2}\ {\rm cm}. \tag{1.17}$$

Above this radius, the optical depth for the electron scattering can be estimated by $\tau \sim n_{\rm e}\sigma_{\rm T} r/\Gamma$, where $n_{\rm e}$ is the electron number density and the assumption of $n_{\rm e} = n_{\rm p}$ leads to $n_{\rm e} \simeq (L_{\rm iso}/4\pi r^2 m_{\rm p} c^3 \Gamma\eta)$. The photosphere is defined by the radius that the optical depth equal to be unity. The dependence of the photospheric radius on the outflow parameters is different whether it is located below or above the saturation radius $r_{\rm s}$ (Mészáros & Rees 2000). If the maximum Lorentz factor η is less than η_* which is defined by

$$\eta_* = \left(\frac{L_{\rm iso}\sigma_{\rm T}}{4\pi m_{\rm p} c^3 r_0}\right)^{1/4} \simeq 10^3 \left(\frac{L_{\rm iso}}{10^{52}\ {\rm erg/s}}\right)^{1/4} \left(\frac{r_0}{10^7\ {\rm cm}}\right)^{-1/4}, \tag{1.18}$$

the photospheric radius is above $r_{\rm s}$. If we denote the photospheric radius for the outflow with $\eta < \eta_*$ by $r_{\rm ph}^{>}$, it can be written as

$$r_{\rm ph}^{>} = \frac{L_{\rm iso}\sigma_{\rm T}}{4\pi m_{\rm p} c^3 \eta^3} \simeq 4.3 \times 10^{11} \left(\frac{L_{\rm iso}}{10^{52}\ {\rm erg/s}}\right) \left(\frac{\eta}{300}\right)^{-3}\ {\rm cm}. \tag{1.19}$$

On the other hand, if the amount of the baryons in the outflow is small and the maximum Lorentz factor exceed a critical value, that is $\eta > \eta_*$, the photospheric radius for this case $r_{\rm ph}^{<}$ is located below the saturation radius and, since the Lorentz factor evolves as $\Gamma \propto r$ is at $r < r_{\rm s}$, $r_{\rm ph}^{<}$ is calculated as

$$\begin{aligned} r_{\rm ph}^{<} &= \left(\frac{L_{\rm iso}\sigma_{\rm T} r_0^2}{4\pi m_{\rm p} c^3 \eta}\right)^{1/3} \\ &\simeq 10^{10} \left(\frac{L_{\rm iso}}{10^{52}\ {\rm erg/s}}\right)^{1/3} \left(\frac{r_0}{10^7\ {\rm cm}}\right)^{2/3} \left(\frac{\eta}{1000}\right)^{-1/3}\ {\rm cm}. \end{aligned} \tag{1.20}$$

If the photospheric radius locates below $r_{\rm p}$, $e^{\pm}$ pairs make the photosphere and the condition can be expressed in terms of η as $\eta > \eta_{\rm p}$ with

$$\eta_{\rm p} \simeq 4 \times 10^6 \left(\frac{L_{\rm iso}}{10^{52}\ {\rm erg/s}}\right)^{1/4} \left(\frac{r_0}{10^7\ {\rm cm}}\right)^{1/2}. \tag{1.21}$$

In this case, the mass ejection rate $\dot{M}$ is quite low

$$\dot{M} \leq 1.4 \times 10^{-9} (L_{\rm iso}/10^{52} {\rm erg\ s^{-1}})(r_0/10^7 {\rm cm})\ M_\odot/s. \tag{1.22}$$

Next, we consider the emissions from the photosphere. Here, we assume the photospheric emission as a blackbody radiation from the photosphere with a matter temperature. If the photospheric radius locates above the saturation radius, i.e., $r_{\rm ph} > r_{\rm s}$, for the case of $\eta < \eta_*$, the Lorentz factor at the photospheric radius $\Gamma_{\rm ph}$ is $\Gamma_{\rm ph} = \eta$. On the other hand, if $\eta > \eta_*$, the photospheric radius locates below the saturation radius, i.e. $r_{\rm ph} < r_{\rm s}$, and from Equation (1.20) the $\Gamma_{\rm ph}$ depends on the location of the photosphere and the maximum Lorentz factor as $\Gamma_{\rm ph} \propto r_{\rm ph} \propto \eta^{-1/3}$. In the case of $\eta > \eta_{\rm p}$, the photosphere is made by $e^{\pm}$ pairs and $\Gamma_{\rm ph}$ depends on $r_{\rm p}$ but not on η, $\Gamma_{\rm ph} = \Gamma(r_{\rm p})$.

Since the radial dependence of the temperature at the photosphere is $kT_{\rm ph} \propto r_{\rm ph}^{-1}$ for $r_{\rm ph} < r_{\rm s}$ and $kT_{\rm ph} \propto r_{\rm ph}^{-2/3}$ for $r_{\rm ph} > r_{\rm s}$, the observed temperature defined by $kT_{\rm ph}^{\rm obs} = kT_{\rm ph}\Gamma_{\rm ph}$ is calculated as

$$\frac{kT_{\rm ph}^{\rm obs}}{kT_0} = \begin{cases} (r_{\rm ph}/r_{\rm s})^{-2/3} = (\eta/\eta_*)^{8/3}, & \text{for } \eta < \eta_*, r_{\rm ph} > r_{\rm s} \\ 1, & \text{for } \eta > \eta_*, r_{\rm ph} < r_{\rm s}. \end{cases} \tag{1.23}$$

From Equation (1.23), observed temperature $kT_{\rm ph}^{\rm obs}$ is equal to the initial temperature kT_0 for the case of $\eta > \eta_*$ (and hence $r_{\rm ph} < r_{\rm s}$). The dependencies of observed luminosity $L_{\rm ph}$ are $L_{\rm ph} \propto r_{\rm ph}^2\Gamma^2(kT_{\rm ph})^4 \propto$ const for $r_{\rm ph} < r_{\rm s}$ and $L_{\rm ph} \propto r_{\rm ph}^{-2/3}$ for $r_{\rm ph} > r_{\rm s}$, that is

$$\frac{L_{\rm ph}}{L_{\rm iso}} = \begin{cases} (r_{\rm ph}^{>}/r_{\rm s})^{-2/3} = (\eta/\eta_*)^{8/3}, & \text{for } \eta < \eta_*, r_{\rm ph} > r_{\rm s} \\ 1, & \text{for } \eta > \eta_*, r_{\rm ph} < r_{\rm s} \end{cases} \tag{1.24}$$

From Equation (1.24), if the amount of the baryons in the outflow is sufficiently small to satisfy the condition $\eta > \eta_* \sim 1000$, the photospheric emission from the fireball can establish the high efficiency of the radiation. However, if the amount of the baryons is relatively large and the outflow has only the moderate value of the maximum Lorentz factor, the the photospheric emission from the fireball has very low efficiency, e.g. $L_{\rm ph}/L_{\rm iso} \sim 2 \times 10^{-3}$ for the case of $\eta \sim 100$. This is because that, if the maximum Lorentz factor η is lower than the critical value η_*, the emission takes place above the saturation radius where the initial thermal energy has been already converted into the kinetic energy of the outflow.

1.3.3 Internal Shock Model

In Section 1.3.2, we mentioned that the photospheric emission from fireball can be emitted only with low efficiency $L_{\rm ph}/L_{\rm iso} < 1\%$ except for the case of very high maximum Lorentz factor. On the other hand, observations of some bursts show very high radiative efficiency of $> 50\%$. In order to achieve such high radiative efficiency, the bulk kinetic energy of the outflow should be dissipated and re-converted into the random energy of the electrons.

Another proposed radiation mechanism is a synchrotron emission from the electrons accelerated by the shock waves (e.g., Meszaros & Rees 1993; Rees & Meszaros 1994; Katz 1994). The shock wave naturally dissipate the bulk kinetic energy of the jet into random energy of the electrons, and the random energy will be released from the jet in the form of the radiation.

If there are some shells with different velocity in the outflow, these shells will collide with each other and produce shock waves. The shock waves are called as internal shocks. In addition, when the ejecta expands and runs into the external medium, the medium will be accumulated ahead of the ejecta and the shock wave, which is called external shocks, will be produced.

In particular, the internal shock model which explains the prompt emission with the synchrotron emission emitted by the electrons accelerated at the internal shocks have been actively studied by many papers (e.g., Rees & Meszaros 1994; Katz 1994; Piran 2004, for review). The internal shock model together with the external shock model for the afterglow (e.g., Meszaros & Rees 1993; Sari et al. 1998) is a the standard scenario for GRBs. In this section, we describe the internal shock model. We also discuss some problems on this model.

Radiative Efficiency

We consider a collision of two shells with different velocities and estimate the efficiency of the energy conversion by the collision (Kobayashi et al. 1997; Katz 1997).

We denote the shell with a higher velocity by the subscript "f", e.g., Lorentz factor of the faster shell is $\Gamma_{\rm f}$, and the slower shell by the subscript "s". When the faster shell catches up the slower shell, they collide and merge into a shell whose mass is the sum of the two shells. The shell created in consequence of the merging of two shells is denoted by the subscript "m" (Figure 1.11). The conservation of the energy and

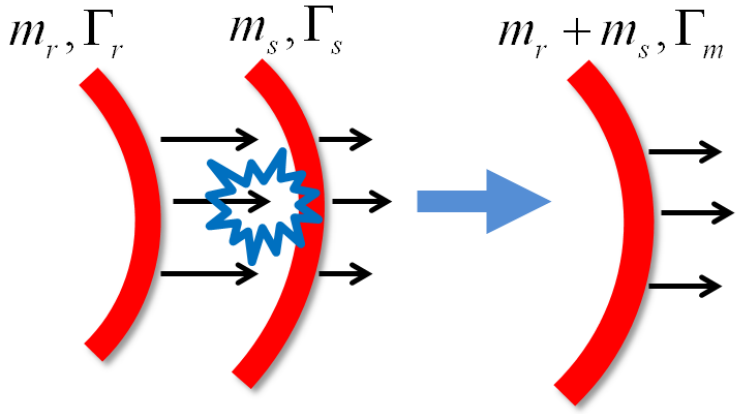

Figure 1.11 A schematic picture of the collision of two shells.

the momentum during the merging is written as

$$m_{\rm r}\Gamma_{\rm r} + m_{\rm s}\Gamma_{\rm s} = (m_{\rm r} + m_{\rm s} + E'_{\rm int}/c^2)\Gamma_{\rm m} \quad (1.25)$$

$$m_{\rm r}\sqrt{\Gamma_{\rm r}^2 - 1} + m_{\rm s}\sqrt{\Gamma_{\rm s}^2 - 1} = (m_{\rm r} + m_{\rm s} + E'_{\rm int}/c^2)\sqrt{\Gamma_{\rm m}^2 - 1}, \quad (1.26)$$

where $E'_{\rm int}$ is a internal energy in the rest-frame of shell "m" released by the collision. Since we here consider the internal shock in a ultra relativistic flow, $\Gamma_{\rm s}$ and $\Gamma_{\rm m}$ are expected to be much larger than unity, i.e., $\Gamma_{\rm m} > \Gamma_{\rm s} \gg 1$. Since the released internal energy by the collision in the observer frame is the change of the kinetic energy before and after the collision, we have the following equation

$$E_{\rm int} = m_{\rm r}c^2(\Gamma_{\rm r} - \Gamma_{\rm m}) + m_{\rm s}c^2(\Gamma_{\rm s} - \Gamma_{\rm m}). \quad (1.27)$$

From the Equation (1.27), the efficiency by which the kinetic energies are converted into the internal energy $\varepsilon \equiv E_{\rm int}/(m_{\rm r}\Gamma_{\rm r}c^2 + m_{\rm s}\Gamma_{\rm s}c^2)$ is calculated by

$$\varepsilon = 1 - \frac{(m_{\rm r} + m_{\rm s})\Gamma_{\rm m}}{m_{\rm r}\Gamma_{\rm r} + m_{\rm s}\Gamma_{\rm s}}. \quad (1.28)$$

If the Lorentz factor of the faster shell $\Gamma_{\rm r}$ is much larger than that of the slower shell $\Gamma_{\rm s}$, i.e., $\Gamma_{\rm r} \gg \Gamma_{\rm s}$, and the masses of two shells are comparable, i.e., $m_{\rm r} \sim m_{\rm s}$, then the efficienfy can be high. For example, if $\Gamma_{\rm r} = 10\Gamma_{\rm s}$ and $m_{\rm r} = m_{\rm s}$, the efficiency can reaches $\varepsilon \sim 40\%$.

Energy Spectrum

Next we consider the energy spectrum in the internal shock model.

The densities and the temperatures in the upstream and downstrem of a relativistic shock wave have following relations (e.g., Johnson & McKee 1971; McKee & Colgate 1973)

$$\begin{aligned} n_2 &= (\Gamma_{21}+3)n_1 \simeq 4\Gamma_{21}n_1 \\ e_2 &= (\Gamma_{21}-1)n_2 m_{\rm p}c^2 \simeq \Gamma_{21}n_2 m_{\rm p}c^2 \simeq 4\Gamma_{21}^2 n_1 m_{\rm p}c^2, \end{aligned} \tag{1.29}$$

where variables in the upstream and the downstream of the shock wave are expressed by the subscripts "1" and "2", respectively. A variable Γ_{21} is the relative Lorentz factor between the upstream and the downstream, and if it is much larger than unity $\Gamma_{21} \gg 1$, the Lorentz factor of the shock surface $\Gamma_{\rm sh}$ is almost same as Γ_{21}, i.e., $\Gamma_{\rm sh} \simeq \Gamma_{21}$. If the electrons and the magnetic field posses portions of the internal energy in the downstrem with $\epsilon_{\rm e}$ and $\epsilon_{\rm B}$, the energies posses by the electrons $e_{\rm e}$ and the magnetic field $e_{\rm B}$ in the downstream are

$$e_{\rm e} \equiv \epsilon_{\rm e} e_2 \simeq 4\Gamma_{21}\epsilon_{\rm e} n_1 m_{\rm p}c^2 \tag{1.30}$$

$$e_{\rm B} = B^2/8\pi \equiv \epsilon_{\rm B} e_2 \simeq 4\Gamma_{21}\epsilon_{\rm B} n_1 m_{\rm p}c^2. \tag{1.31}$$

We assume that $\epsilon_{\rm e}$, $\epsilon_{\rm B}$ are constant during the burst.

We consider the synchrotron emission from an electron whose Lorentz factor is $\gamma_{\rm e}$. Since the characteristic frequency of the synchrotron emission is calculated by $\nu = \hbar e B\gamma_{\rm e}^2/m_{\rm e}c$ (e.g., Rybicki & Lightman 1979), the emission is observed with following characteristic frequency

$$(h\nu)_{\rm obs} = \frac{\hbar e B}{m_{\rm e}c}\gamma_{\rm e}^2\Gamma. \tag{1.32}$$

It is widely known that the electrons accelerated at the strong shock wave by the first order Fermi acceleration have a power-law distribution (e.g., Blandford & Eichler 1987). Thus we assume the distribution function of the electrons as

$$N(\gamma_{\rm e})d\gamma_{\rm e} \propto \gamma_{\rm e}^{-p} d\gamma_{\rm e} \quad \text{for } \gamma_{\rm e} > \gamma_{\rm e,m}, \tag{1.33}$$

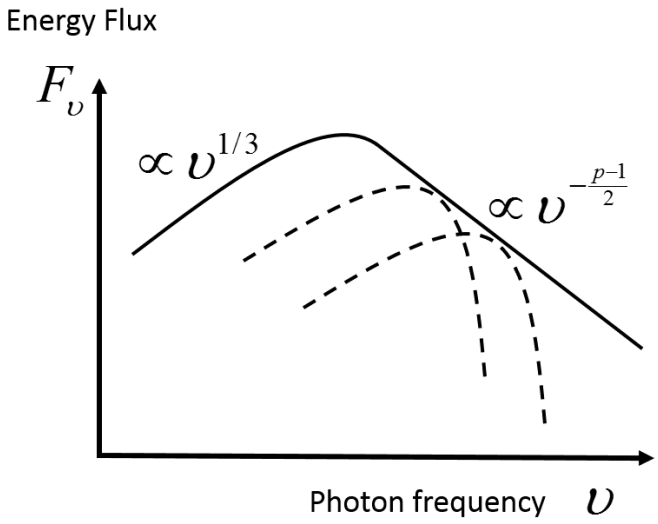

Figure 1.12 A schematic picture of the spectrum from power-law distributed electrons.

where p is a power-law index which is predicted to be $p > 2$ by the shock acceleration theory and $\gamma_{\rm e,m}$ is a minimum Lorentz factor only above which the electrons have a power-law distribution. The following relation between $\gamma_{\rm e}$ and $e_{\rm e}$ holds (e.g., Sari et al. 1996)

$$\gamma_{\rm e,m} = \left(\frac{p-2}{p-1}\right)\frac{e_{\rm e}}{\xi_{\rm e} n_2 m_{\rm e} c^2} \simeq \frac{\epsilon_{\rm e}}{\xi_{\rm e}}\left(\frac{p-2}{p-1}\right)\frac{m_{\rm p}}{m_{\rm e}}\Gamma_{21}, \tag{1.34}$$

where $\xi_{\rm e}$ is the fraction of the accelerated electrons (Bykov & Meszaros 1996). If we assume $p = 2.5$ (Sari et al. 1996), $\gamma_{\rm e,m}$ becomes $\gamma_{\rm e,m} \simeq 6 \times 10^3 \epsilon_{\rm e,-1}\xi_{\rm e,-1}\Gamma_{21}$.

Since the spectrum of the synchrotron emission from electrons with the power-law distribution with index of p is also power-law with the index of $-(p-1)/2$ (e.g., Rybicki & Lightman 1979), the spectral index is expected to be $-(p-1)/2$ above the frequency which corresponds to $\gamma_{\rm e,m}$, i.e., above $\nu_{\rm m} \equiv \hbar e B \gamma_{\rm e,m}^2 \Gamma / m_{\rm e} c$. On the other hand, the spectral index below $\nu_{\rm m}$ is determined by the low frequency part of the synchrotron emission from one electron, which have an index of 1/3. Thus, the

observed spectrum around $\nu_{\rm m}$ is predicted to be

$$F_\nu \propto \begin{cases} \nu^{1/3} & \text{for } \nu < \nu_{\rm m}, \\ \nu^{-(p-1)/2} & \text{for } \nu > \nu_{\rm m}. \end{cases} \tag{1.35}$$

The observed peak energy can be estimated from Equation (1.31) (1.32), and (1.34) with the parameters for the internal shock as

$$(h\nu_{\rm m})_{\rm obs} \sim 400 \left(\frac{\epsilon_{\rm B}}{0.1}\right)^{1/2} \left(\frac{\epsilon_{\rm e}}{0.1}\right)^{2} \left(\frac{\xi_{\rm e}}{0.1}\right)^{-2} \left(\frac{n_{\rm e}}{10^{12}\ {\rm cm}^{-3}}\right)^{1/2} \left(\frac{\Gamma}{300}\right)\ {\rm keV}, \tag{1.36}$$

where we assume $\Gamma_{21} \sim 1$. This peak energy is well consistent with the observational typical value of the prompt emission (see Figure 1.7).

Problems of the Internal Shock Model

In the previous sections, we described the efficiency of energy conversion ($\sim$ radiative efficiency) and the radiation spectrum from the internal shocks. However, the internal shock model has some problems in both the radiative efficiency and the energy spectrum.

If one consider a collision of two shells, the radiative efficiency can be reached as high as $\sim 40\%$ if the ratio of the Lorentz factor of two shells is ~ 10 and the masses of them is comparable. Howerver, the light curves of the prompt emission have very rapid time variabilities, which indicates that there should be a lot of collisions of shells in a bursts. The radiative efficiency in such a circumstance is estimated by the sum of the energy conversions from kinetic energy into the internal energy

$$\epsilon = 1 - \frac{\Sigma m_{\rm i}^{\rm (f)} \gamma_{\rm i}^{\rm (f)}}{\Sigma m_{\rm i}^{\rm (i)} \gamma_{\rm i}^{\rm (i)}}. \tag{1.37}$$

Here, the sum is calculated for the entire shells. The superscribe (f) and (i) indicate that the values are for the one after and before the collisions, respectively.

Kobayashi et al. (1997) calculated the radiative efficiency with Equation (1.37) for various parameters. Figure 1.13 shows a result of the calculation with 500 shells. From their results, if the energies possessed by the all shells are the same and the ratio of largest and smallest Lorentz factors of the shells $\gamma_{\rm max}/\gamma_{\rm min}$ is very large, e.g.,

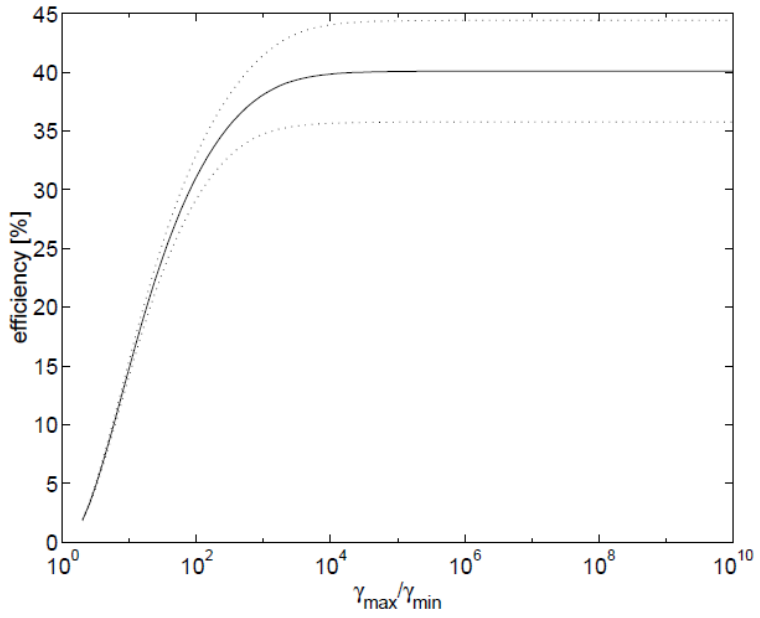

Figure 1.13 The efficiency of the energy conversion ($\sim$ radiative efficiency) by the collisions of 500 shells as a function of the ratio of largest and smallest Lorentz factors of the shells calculated by Kobayashi et al. (1997). The energy possessed by the shells is assumed to be the same and the smallest Lorentz factor of the shells is fixed to be $\gamma_{\rm min} = 10$.

$\gamma_{\rm max}/\gamma_{\rm min} > 10^3$, the efficiency can reache $\sim 30\%$. However, if the ratio of the largest and the smallest Lorentz factors is not so large, e.g., $\gamma_{\rm max}/\gamma_{\rm min} < 10$, the efficiency will be $\epsilon < 10\%$. On the other hand, as mentioned in Section 1.2.1, some bursts shows the radiative efficiencies of $\epsilon > 50\%$ and it is difficult to explain such high radiative efficiencies with the internal shock model.

In addition, we mentioned that the low energy spectral index from power-law distributed electrons is 1/3 which corresponds to a low energy photon index of -2/3. If one consider the emission in more detail, harder spectral index at the low energy side is possible. However, the low energy spectral index harder than 1/3 cannot be explained by the optically thin synchrotron emission. On the other hand, a portion of the bursts actually exhibit such hard low energy spectral index and this is called as "line of death problem" of the prompt emission (Preece et al. 1998).

1.3.4 Photospheric Model

In the previous section, we discussed the problems of the internal shock model. In this section, we describe an another model which, called photspheric model, which is recentlly attracts attensions from both theoretical and observational view.

For example, Ryde et al. (2010) argued that the spectrum of GRB 090902B can be well fitted by a quasi-blackbody with a characteristic temperature of ~ 290 keV. Moreover, it has been reported that some bursts exhibit a thermal component on a usual non-thermal component (e.g., Guiriec et al. 2011; Axelsson et al. 2012). These observations indicate that the thermal component may appear in the spectrum as a blackbody spectrum, aside from its dominance in the spectrum. However, it is not clear whether the thermal emission always appears in the spectrum as a blackbody like spectrum or not. Themal emission may appear with a non-thermal behavior by some mechanisms (see below). Therefore, investigation of the thermal radiation from GRB jets is crucial to understand the radiation mechanism of GRBs.

As mentioned in Section 1.3.2, photospheric emission from an adiabatically expanding fireball have only a small radiative efficiency, unless the Lorentz factor of the fireball is larger than a critical value η, i.e., $\eta > \eta_*$ (see Equation (1.24)). However, if the kinetic energy of the flow is disippated by some sort of mechanism, some fraction of the kinetic energy $\epsilon_{\rm d} < 1$ will be re-converted into thermal energy. In this case, the radiation energy, which decreases as $L_\gamma \propto (r/r_{\rm s})^{-2/3}$ without dissipation, will in-

crease as $L_\gamma \sim \epsilon_{\rm d} > L_0(r/r_{\rm s})^{-2/3}$ (Rees & Mészáros 2005). Moreover, the high energy power-law tail, which does not exist on the spectrum of thermal emission from adiabatically expanding fireball, could appear due to the inverse Compton scatterings by the non-thermal electrons energized by the dissipation, which may explain the observed high energy slope of GRB spectrum (see Figure 1.6). Some mechanisms of the dissipation process have been suggested so far. For example, Beloborodov (2010) suggested that free neutrons possibly contained in the jet might have a crucial role for the prompt emission. They argued that the neutrons will collide with protons component below the photosphere, which disspates the bulk kinetic energy into the non-thermal, high-energy electron energies via inelastic nuclear scatterings between neutrons and protons. Giannios (2006, 2008, 2012) investigated the spectrum of thermal emission from magnetized outflow assuming that the magnetic field energy is gradually dissipated via magnetic reconnection and argued that such mechanism can explain the observed spectrum.

On the other hand, geometrical structures of the jet must be considered in the calculations of thermal emission since GRB outflows have jet-like structures with finite opening angles in reality. For example, Lundman et al. (2013) investigated photospheric emission from a conical jet whose Lorentz factor decreases with the angle from the jet axis. They suggested that the low energy part of GRB spectrum could be the emission from outer edge of the jet. Ito et al. (2013) investigated photospheric emission from stratified jet which consists of a highly relativistic spine region and the surrounding less relativistic sheath region. They suggested that, when a photon intersects the boundary between spine and sheath regions, it gains energies via the electron scatterings and the high energy tail of the observed spectrum can be explained by the photons which energized by the such mechanism.

Photospheric emission from the relativistic jet from a massive star with realistic structures calculated with the relativistic multi-dimensional hydrodynamics simulations have also been investigated by some authors (Lazzati et al. 2009, 2011; Nagakura et al. 2011; Mizuta et al. 2011). Especially, Lazzati et al. (2009) suggested that shock wave generated by the interaction between the jet and the star dissipates the bulk kinetic energy of the jet into the internal energy and it makes the photospheric emission highly efficient ($\eta \sim 50\%$). They calculated thermal emission just by superposing blabkbody emissions from the photosphere. However, the observed photons should be produced in inner regions with $\tau_{\rm s} \gg 1$ (Beloborodov 2013; Vurm et al. 2013) since the

radiation and absorption processes are inefficient near the photosphere with $\tau_{\rm s} = 1$, where $\tau_{\rm s}$ is a optical depth for electron scattering, due to the low plasma density. The produced photons propagate through the jet and cocoon which have complicated structure. Thus, a radiative transfer calculation that properly evaluate the photon production site is necessary to investigate the thermal radiation from GRB jets.

CHAPTER 2
METHODS FOR NUMERICAL CALCULATIONS

2.1 Monte-Carlo Radiative Transfer Code

Here, we descibe the numerical code for a relativistic radiative transfer calculation. The code is based on the Monte-Carlo method and calculate photon transfer with random numbers. The special relativistic effects are fully taken into account in the code.

2.1.1 Photon Transfer with Monte-Carlo Method

We describe the method to treat the photon transfer in uniform medium which has a relativistic velocity in the laboratory frame. Of course, the structure of GRB jets are not uniform but if we consider sufficiently small regions the plasma can be treated as a uniform flow.

We suppose that the electrons in the plasma has a velocity $\beta_{\rm e}$ in the laboratory frame, which is calculated with considering both bulk fluid motion and thermal motion of the electron. The thermal motion of the electron is determined with random numbers as to obey relativistic Maxwell distribution and is assumed to be isotropic in fluid comoving frame. The number density of electrons in the laboratory frame is denoted by $n_{\rm e}$.

The optical depth for a photon during a travel of small distance δs is $\delta\tau = \Gamma_{\rm e}(1 - \beta_{\rm e}\cos\theta)n_{\rm e}\sigma\delta s$, where $\Gamma_{\rm e}$ is the Lorentz factor of the electron, $\Gamma_{\rm e} = 1/\sqrt{1-\beta_{\rm e}^2}$, and θ is the angle between the directions of electron motion and the propagation of photon in laboratory frame. The probability $P_{\rm s}$ that a photon scatters on $\delta\tau$ is calculated by

$$P_{\rm s} = 1 - e^{-\delta\tau}. \tag{2.1}$$

The occurrence of scattering during the travels of δs is evaluated with a uniform random number R_1 with a range of 0-1. If $R_1 > P_{\rm s}$, the scattering does not occur and the photon freely travels the distance δs. On the other hand, if $R_1 < P_{\rm s}$, the photon is scattered by an electron at a distance $l_{\rm s} < \delta s$, which is calculated with R_1 as

$$l_{\rm s} = \frac{-\ln(1-R_1)}{\Gamma_{\rm e}(1-\beta_{\rm e}\cos\theta)n_{\rm e}\sigma}. \tag{2.2}$$

We use the Klein-Nishina total cross section $\sigma_{\rm KN}$ for σ, which is calculated by

$$\sigma_{\rm KN} = \sigma_{\rm T}\frac{3}{4}\left[\frac{1+x}{x^3}\left\{\frac{2x(1+x)}{1+2x} - \ln(1+2x)\right\} + \frac{1}{2x}\ln(1+2x) - \frac{1+3x}{(1+2x)^2}\right], \quad (2.3)$$

where $\sigma_{\rm T}$ and x are the total cross section for Thomson scattering and the energy of a photon in electron restframe divided by the electron rest mass energy, $x = h\nu'/m_{\rm e}c^2$.

2.1.2 Treatment of Scatterings

If a scattering occured, the energy and the propagation direction of a photon is altered by the scattering. We describe the way to calculate the 4-momentum of a photon after the scattering.

The scatterings are calculated in the electron restframe since the treatment of the scatterings is much easier than that in the laboratory frame. We Lorentz-transform the 4-momentum of a photon before scattering in the laboratory frame into the electron restframe, calculate the scattering in the electron restframe, and then we get the 4-momentum of the photon after the scattering in the laboratory frame by Lorentz-transform the 4-momentum into the laboratory frame again.

We consider the frame in which the electron is at rest at the origin of the coordinate and the photon propagates toward z'-direction before the scattering. The photon has the 4-momentum $p_{\rm i}'^{\mu}$ before the scattering and $p_{\rm f}'^{\mu}$ after the scattering. If we denote the energy of the photons before and after the scattering in this frame as $e_{\rm i}'$ and $e_{\rm f}'$, $p_{\rm i}'^{\mu}$ and $p_{\rm f}'^{\mu}$ is written as

$$p_{\rm i}'^{\mu} = \frac{e_{\rm i}'}{c}\begin{pmatrix}1\\0\\0\\1\end{pmatrix}, \qquad p_{\rm f}'^{\mu} = \frac{e_{\rm f}'}{c}\begin{pmatrix}1\\ \sin\theta_{\rm f}'\cos\phi_{\rm f}'\\ \sin\theta_{\rm f}'\sin\phi_{\rm f}'\\ \cos\theta_{\rm f}'\end{pmatrix}, \quad (2.4)$$

where $\theta_{\rm f}'$ and $\phi_{\rm f}'$ are the zenith and azimuthal angles with which the potons propagate after the scattering in this frame (Figure 2.1). The three variables of $e_{\rm i}'$, $e_{\rm f}'$, and $\theta_{\rm f}'$ are related each other with these equations,

$$e_{\rm f}' = \frac{e_{\rm i}'}{1 + \frac{e_{\rm i}'}{m_{\rm e}c^2}(1-\cos\theta_{\rm f}')} \quad (2.5)$$

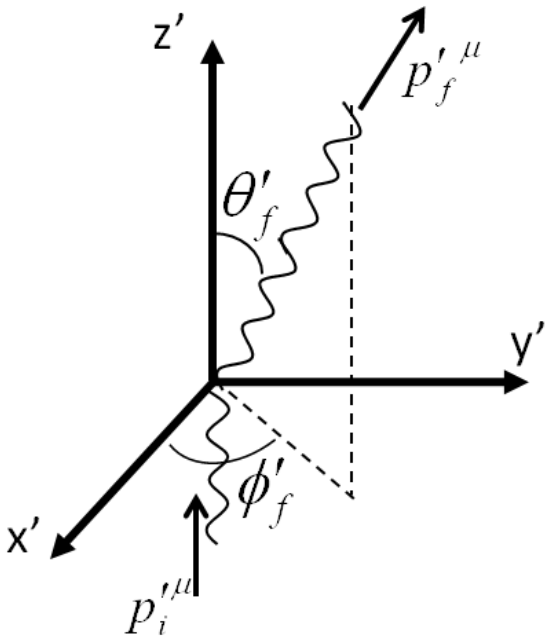

Figure 2.1 Schematic picture.

and

$$\frac{d\sigma_{\mathrm{KN}}}{d\Omega} = \frac{r_0^2}{2}\frac{e_{\mathrm{i}}'^2}{e_{\mathrm{f}}'^2}\left(\frac{e_{\mathrm{f}}'}{e_{\mathrm{i}}'} + \frac{e_{\mathrm{i}}'}{e_{\mathrm{f}}'} - \sin^2\theta_{\mathrm{f}}'\right), \tag{2.6}$$

where r_0 is the classical electron radius and we adopt the Klein-Nishina differential cross section. If we eliminate e_{f}' in Equation (2.6) by substituting Equation (2.5), we can express $d\sigma_{\mathrm{KN}}/d\Omega$ as functions of e_{i}' and θ_{f}'. Since e_{i}' is given, we can obtain θ_{f}' as to obey $d\sigma_{\mathrm{KN}}/d\Omega$ with random numbers. We can also obtain ϕ_{f}' with a uniform random number between 0 to 2π. Then, we calculate e_{f}' from Equation (2.5) and get $p_{\mathrm{f}}'^{\mu}$ from Equation (2.4).

The above procedure to calculate the 4-momentum of a photon after a scattering is considered in the coordinate system in which the photon propagate toward z'-direction before the scattering. If the photon has a propagation direction with θ and ϕ in the electron restframe, we get the 4-momentum of the photon after the scattering by rotating $p_{\mathrm{f}}'^{\mu}$ by θ and ϕ.

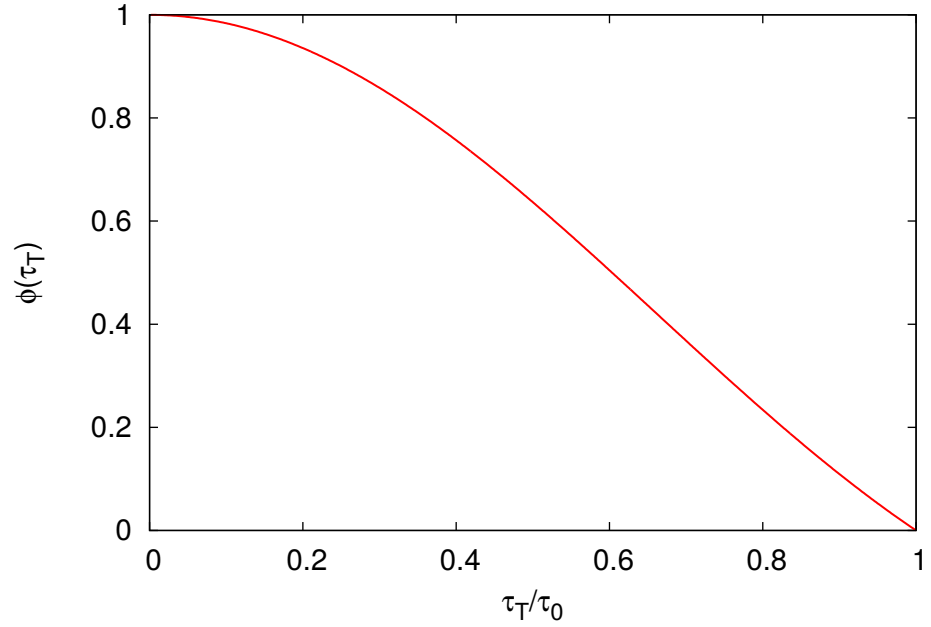

Figure 2.2 The spatial distribution of the injected photons as a function of $\tau_{\rm T}/\tau_0$.

2.1.3 Test Calculations

Here, we tests the numerical code by calculations of thermal Comptonization in a spherical hot cloud which has a constant temperature and density. An analytic formula of the energy spectrum of the radiation from such hot spherical cloud have been derived in Sunyaev & Titarchuk (1980).

In the calculations, the cloud has a radius R, electron temperature $T_{\rm e}$, and electron number density $n_{\rm e}$. The Thomson optical depth of the cloud is defined by $\tau_0 \equiv n_{\rm e}\sigma_{\rm T}R$. The photons with energies much smaller than the electron thermal energy, i.e., $h\nu_0 = 0.1{\rm eV} \ll kT_{\rm e}$ are injected with the spatial distribution function $\phi(\tau_{\rm T})$ defined by

$$\phi(\tau_{\rm T}) = \frac{\tau_0}{\pi\tau_{\rm T}} \sin\frac{\pi\tau_{\rm T}}{\tau_0}, \tag{2.7}$$

where $\tau_{\rm T}$ is the Thomson optical depth measured from the center of the cloud (Figure 2.2).

The analytical solution for this problem for $h\nu \gg h\nu_0$ is written as

$$F(x) = Ax^3e^{-3}\int_0^\infty t^{\alpha-1}e^{-t}\left(1+\frac{t}{x}\right)^{\alpha+3} dt, \tag{2.8}$$

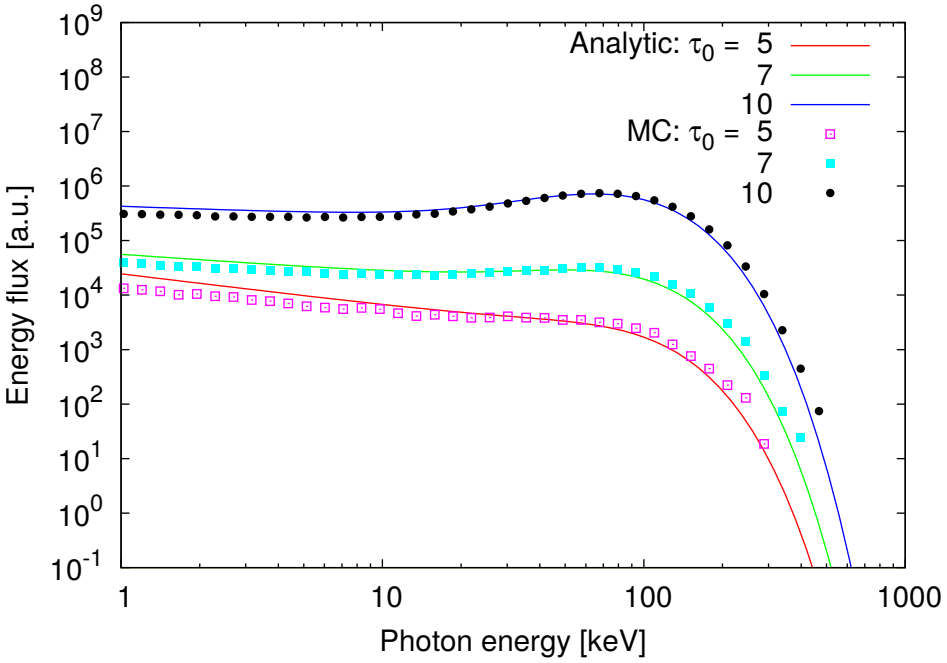

Figure 2.3 Results of the test calculations of Monte-Carlo code. The results represented by dots are compared with the analytic solutions (Eq. 2.8).

where x is the photon energy devided by the electron thermal energy $x \equiv h\nu/kT_{\rm e}$, A is a normalization factor, and α is

$$\alpha = \left(\frac{9}{4} + \gamma\right)^{1/2} - \frac{3}{2}, \qquad \gamma = \frac{\pi^2 m_{\rm e} c^2}{3(\tau_0 + \frac{2}{3})^2 kT_{\rm e}}. \tag{2.9}$$

The spectrum has a shape of a power-law with the index of α at $x \ll 1$. Since the Thomson cross section is used for the differential and total scattering cross sections in the derivation of the analytical formula, we also use the Thomson cross section in the test calculations of Monte-Carlo radiative transfer code.

Figure 2.3 shows the results of the calculations with the clouds whose Thomson optical depths are 5, 7, and 10. The analytic solutions (Eq. 2.8) are also shown in Figure 2.3. It can be seen that there is good agreement between the results of Monte-Carlo calculations and the analytic solutions.

2.2 Special Relativistic Hydrodynamics Code

We calculate the structure of the relativistic jet from massive progenitor star by a relativistic hydrodynamics simulation (Chapter 4). In this section, we describe a multi-dimensional special relativistic hydrodynamics code (Tominaga 2009) used for the hydrodynamics simulation. We apply the unit system that the speed of light equal to unity, i.e., $c = 1$, in this section.

2.2.1 Basic Equations

The equations of special relativistic hydrodynamics can be written by a fluid four-velocity u^μ and an energy momentum tensor (Marti & Muller 1994). Here, we express the equations with following conserved quantities: relativistic rest-mass density D, the i-th component of momentum density $S_{\rm i}$, and energy density τ defined by

$$D \equiv \rho\Gamma, \tag{2.10}$$

$$S_{\rm i} \equiv \rho h\Gamma^2 v_{\rm i}, \tag{2.11}$$

$$\tau \equiv \rho h\Gamma^2 - p - \rho\Gamma, \tag{2.12}$$

where ρ is the fluid rest-frame density, p is the pressure, and h is the specific enthalpy which is defined by

$$h = 1 + \varepsilon + \frac{p}{\rho}. \tag{2.13}$$

With these quantities, the equations of relativistic hydrodynamics with newtonian gravity in two-dimensions (assuming axisymmetry) are approximately expressed as (Tominaga 2009)

$$\frac{\partial D}{\partial t} + \frac{1}{r^2}\frac{\partial (r^2 D v_{\rm r})}{\partial r} + \frac{1}{r\sin\theta}\frac{\partial (\sin\theta D v_\theta)}{\partial \theta} = 0, \tag{2.14}$$

$$\frac{\partial S_{\rm r}}{\partial t} + \frac{1}{r^2}\frac{\partial \{r^2(S_{\rm r} v_{\rm r} + p)\}}{\partial r} + \frac{1}{r\sin\theta}\frac{\partial (\sin\theta S_{\rm r} v_\theta)}{\partial \theta} = \frac{2p}{r} + \frac{S_\theta v_\theta}{r} + g_{\rm r}\rho, \tag{2.15}$$

$$\frac{\partial S_\theta}{\partial t} + \frac{1}{r^2}\frac{\partial (r^2 S_\theta v_{\rm r})}{\partial r} + \frac{1}{r\sin\theta}\frac{\partial \{\sin\theta(S_\theta v_\theta + p)\}}{\partial \theta} = -\frac{S_\theta v_{\rm r}}{r} + \frac{p}{r}\cot\theta + g_\theta\rho, \tag{2.16}$$

$$\frac{\partial \tau}{\partial t} + \frac{1}{r^2}\frac{\partial \{r^2(S_{\rm r} - D v_{\rm r})\}}{\partial r} + \frac{1}{r\sin\theta}\frac{\partial \{\sin\theta(S_\theta - D v_\theta)\}}{\partial \theta} = (g_{\rm r} v_{\rm r} + g_\theta v_\theta)\rho, \tag{2.17}$$

where $g_{\rm r}$ and g_θ are the radial and the angular components of graviational acceleration,

respectively.

We use a special relativistic hydrodynamics code with Marquina's flux formula (Donat et al. 1998) and with a conversion method from the observer frame to the fluid rest frame (Martí & Müller 1996). The third-order Runge-Kutta method developed by Shu & Osher (1988) is applied for the time integration and the second-order piecewise hyperbolic method (PHM) developed by Marquina et al. (1992) is applied for the spatial interpolation. The contributions from self-gravity is taken into account with the use of a Poisson equation solver (Hachisu 1986).

2.2.2 Equation of State

We adopt an equation of state for relativistic particles, i.e., $e_{\rm int} = p/(\gamma - 1)$ with $\gamma = 4/3$, where $e_{\rm int}$ and γ are the rest-frame internal energy and the adiabatic index, respectively, since the fluid is radiation dominated in the environment we consider in this thesis. Temperature T is derived taking into account both the radiation and the e^+e^- pairs by following equation (e.g., Freiburghaus et al. 1999):

$$e_{\rm int} = aT^4 \left(1 + \frac{7}{4}\frac{T_9^2}{T_9^2 + 5.3}\right), \tag{2.18}$$

where $a = 7.57 \times 10^{-15}$ erg cm^{-3} K^{-4} is the radiation constant and $T_9 = T/(10^9$ K).

CHAPTER 3
RANDOM WALKS OF PHOTONS IN RELATIVISTIC FLOW

3.1 Overview

Relativistic flows or jets are important phenomena in many astrophysical objects, such as gamma-ray bursts (GRBs) and active galactic nuclei (AGNs). It is widely accepted that most of high-energy emission from these objects arises from the relativistic jets. However, their radiation mechanism is not fully understood. In particular, recent observations of GRBs have indicated the existence of thermal radiation in the spectrum of the prompt emission, which casts a question to standard emission models invoking synchrotron emission.

As mentioned in Section 1.3.4, to study the thermal radiation, treatment of the photosphere needs careful consideration. Lazzati et al. (2009, 2011); Mizuta et al. (2011); Nagakura et al. (2011) performed the hydrodynamical simulations of relativistic jet and calculated the thermal radiation assuming that the photons are emitted at the photosphere which is defined by the optical depth for electron scattering $\tau_{\rm s} = 1$. However, the observed photons should be produced in more inner regions with $\tau_{\rm s} \gg 1$ (e.g., Beloborodov 2013) since the radiation and absorption processes are very inefficient near the photosphere due to the low plasma density. The produced photons propagate through the jet and cocoon which have complicated structure. Thus, radiative transfer calculation of the propagating photons properly evaluating the photon production site is necessary to investigate the thermal radiation from GRB jets.

The photon production site can be estimated by the effective optical depth τ_* (e.g., Rybicki & Lightman 1979). However, the expression derived in Rybicki & Lightman (1979) is based on an assumption that each scatterings is isotropic in observer frame. The assumption does not strictly hold in any moving media because the photon propagation is concentrated to the direction of the flow due to the beaming effect in the observer frame (Figure 3.1).

In this chapter, we construct an expression for the effective optical depth considering the random walk process in the relativistic flow. In Section 3.2, we analytically investigate the random walk process in relativistic flow and present the expression for the effective optical depth. In Section 3.2.3, we demonstrate that the number of

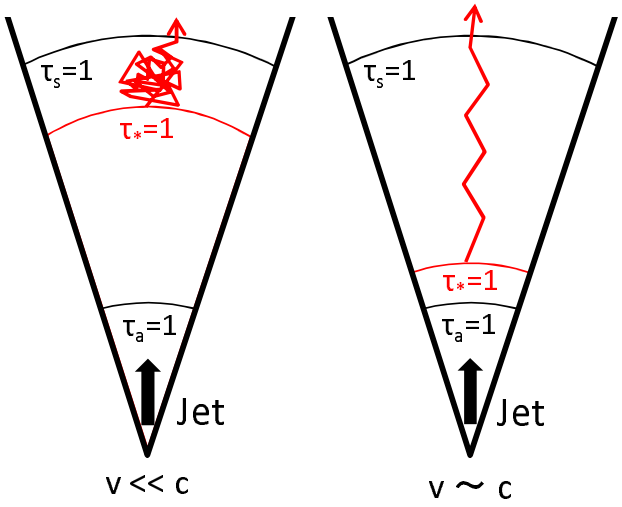

Figure 3.1 Schematic pictures of photon propagation in the jet with the velocity $v \ll c$ (left) and $v \sim c$ (right). When $v \ll c$, the scatterings of the photons are approximately isotropic in the observer frame and the surface of $\tau_* = 1$ is located far from the surface of $\tau_{\rm a} = 1$, where $\tau_{\rm a}$ is an optical depth in the absence of the scatterings. When $v \sim c$, the photons are concentrate to the direction of the flow. Thus, the surface of $\tau_* = 1$ is located close to the surface of $\tau_{\rm a} = 1$.

scatterings obtained by the analytic expression agrees with that derived by Monte Carlo simulations. Finally, summary and discussions are presented in Section 3.3.

3.2 Analytic expression of random walks in relativistic flow

In this section, we extend the argument for the random walk process shown in Rybicki & Lightman (1979) to the relativistic flow. For simplicity, we assume that the scatterings are isotropic and elastic in the electron rest frame.

3.2.1 Pure scattering

We first consider purely scattering medium with uniform opacity in which photons are scattered N times. The path of the photons between i-1th and ith scattering is denoted by $\mathbf{r}_i$. The net displacement of the photon after N scatterings is $\mathbf{R} = \mathbf{r}_1 + \mathbf{r}_2 + \cdots + \mathbf{r}_N$. In order to derive the average net displacement of photons l_*, we first take the square of $\mathbf{R}$ and then average it,

$$l_*^2 \equiv \langle \mathbf{R}^2 \rangle = \sum_{i=1}^{N} \langle \mathbf{r}_i^2 \rangle + \sum_{\substack{i,j \\ i \neq j}}^{N} \langle \mathbf{r}_i \cdot \mathbf{r}_j \rangle, \tag{3.1}$$

where the angle bracket indicates the average for all photons.

If the medium is at rest relative to an observer, the second term in right hand side of equation (3.1) vanishes due to the front-back symmetry of the scatterings and only the first term contributes to l_*. In this case, the first term is calculated as $N\langle \overline{\mathbf{r}^2} \rangle$ where $\overline{\mathbf{r}^2}$ is the expected value of the square of the mean free path. Since the probability that a photon travels a distance x is $\exp(-x/l)/l$, where l is the mean free path of the photon, $\overline{\mathbf{r}^2}$ can be calculated as

$$\overline{\mathbf{r}^2} = l^{-1} \int_0^\infty x^2 \exp(-x/l) dx = 2l^2. \tag{3.2}$$

Therefore, since l is the same as the mean free path in the comoving frame l_0 for the static medium and the mean free path is the same for all photons, $l_*^2 = 2N\langle l^2 \rangle = 2N l_0^2$.[1]

[1]This is different from the one shown in the Rybicki & Lightman (1979) by the factor of 2. The

The number of scatterings required for a photon to escape a medium which has a finite width L_0 in the comoving frame is $N = (L_0/l_0)^2/2 = \tau_0^2/2$, where τ_0 is the optical depth of the medium, and this is Lorentz invariant. However, the calculation of the mean number of scatterings of the photons propagating the distance L in the observer frame is more complicated because the distances in the two frames are different and the origin of photon production moves in the observer frame.

The radius is usually measured in the observer frame especially when one performs the hydrodynamical simulations and when the emission radius is observationally measured. Thus, it is useful to construct an expression in the observer frame to describe the diffusion of photons. Therefore, we consider mean number of scatterings while the photons propagate a distance L in the observer frame.

If the medium has a relativistic speed, the second term in right hand side of Equation (3.1) remains because the photons concentrate in the velocity directions of the medium due to relativistic beaming effect. Therefore, the average of scalar products of each path have a non-zero value in the observer frame. Moreover, the average for the first term must take into account the dependence on the angle between the directions of the photon propagation and the flow velocity because the mean free path is angle dependent in the relativistic flow. Thus, in order to treat the random walk process in relativistic flow, we need to estimate both $\langle \mathbf{r}_i^2 \rangle$ and $\langle \mathbf{r}_i \cdot \mathbf{r}_j \rangle$ with taking into account the relativistic effect.

The mean free path of a photon in the observer frame is given as $l = l_0/\Gamma(1 - \beta\cos\theta)$ (Abramowicz et al. 1991), where, Γ, β, and θ are fluid Lorentz factor, fluid velocity in unit of speed of light, and the angle between the directions of photon propagation and fluid velocity, respectively. We average l^2 integrating in the comoving frame as follows[2]

$$\langle l^2 \rangle = \frac{l_0^2}{4\pi\Gamma^2} \int_0^{2\pi} d\phi' \int_0^{\pi} \sin\theta' d\theta' (1 - \beta\cos\theta)^{-2}, \tag{3.3}$$

where the values measured in the comoving frame are denoted with prime. Using the relation between the angles in the observer frame and the comoving frame, that is

difference comes from that the first term in Eq. (3.1) is estimated approximately as Nl^2 in Rybicki & Lightman (1979) but, in this thesis, we calculate the term precisely considering the expected value of the square of the mean free path.

[2]The integration can also be done in the observer frame with weighting by distribution of the photon rays resulted from the beaming effect.

$\cos\theta = (\beta + \cos\theta')/(1 + \beta\cos\theta')$, we obtain

$$\langle l^2 \rangle = \frac{\Gamma^2(\beta^2+3)}{3} l_0^2, \tag{3.4}$$

and the first term in Equation (3.1) is calculated by $2N\langle l^2\rangle$.

The scalar product of two paths is $\mathbf{r}_i \cdot \mathbf{r}_j = l_i l_j(\sin\theta_i \cos\phi_i \sin\theta_j \cos\phi_j + \sin\theta_i \sin\phi_i \sin\theta_j \sin\phi_j + \cos\theta_i \cos\theta_j)$. If we set the polar axis to the direction of the photon propagation, the azimuthal angle ϕ is identical in both frames. Thus only the third term in the bracket contributes the average and we obtain

$$\begin{aligned} \langle \mathbf{r}_i \cdot \mathbf{r}_j \rangle &= \frac{1}{(4\pi)^2} \int d\Omega_i' \int d\Omega_j' \; l_i l_j \cos\theta_i \cos\theta_j \\ &= (\Gamma\beta)^2 l_0^2. \end{aligned} \tag{3.5}$$

Substituting the equation (3.4) and (3.5) into equation (3.1), we obtain

$$l_*^2 = N\frac{2}{3}\Gamma^2(\beta^2+3) l_0^2 + N(N-1)(\Gamma\beta)^2 l_0^2. \tag{3.6}$$

If we set $l_* = L$, N corresponds to the mean number of scatterings during the photons propagation of the net distance L in the observer frame. This leads to a quadratic equation for N as

$$(\Gamma\beta)^2 N^2 + \Gamma^2(2 - \frac{\beta^2}{3})N - \xi^2 = 0, \tag{3.7}$$

where $\xi \equiv L/l_0$ is the size parameter. If the medium is static, ξ corresponds to the optical depth of the medium. However, in general, ξ does not correspond to the optical depth because it is defined by the size of the medium in the observer frame, L, and the mean free path of a photon in the comoving frame, l_0.[3] We employ ξ as the parameter to parametrize the distance in the observer frame. We can derive N by solving Equation (3.7) as

$$N = \frac{1}{2a}(\sqrt{b^2 + 4a\xi^2} - b), \tag{3.8}$$

where $a = (\Gamma\beta)^2$ and $b = \Gamma^2(2 - \beta^2/3)$.

We derive important indications from equation (3.8) as follows: When $\xi^2 \ll b^2/4a$,

[3]Since the mean free path in the observer frame depends on the angle between the direction of photon propagation and the flow velocity, we define ξ with L and l_0.

which approximately means $\beta/\Gamma \ll \xi^{-1}$, N reduces to ξ^2/b and $N \simeq \xi^2/2$ for non-relativistic flow[4]. However, if $\xi^2 \gg b^2/4a$, which means $\beta/\Gamma \gg \xi^{-1}$, N becomes $N \simeq \xi/\sqrt{2a} = \xi/\sqrt{2}\Gamma\beta$. Thus, when the beaming is effective and the medium is sufficiently optically thick, N is proportional to ξ with the factor which corresponds to the reduction of the optical depth for relativistic effect. This is because photons propagate approximately straight toward the outside and the number of target electrons during the propagation is proportional to $L \propto \xi$.

It is noted that the ξ is calculated by l_0 which is mean free path in the comoving frame. Equation (3.8) also can be expressed with the optical depth $\tau = \Gamma(1-\beta\cos\Theta)\xi$ instead of ξ as

$$N = \frac{1}{2a}\left(\sqrt{b^2 + \frac{4a\tau^2}{\Gamma^2(1-\beta\cos\Theta)^2}} - b\right), \tag{3.9}$$

where Θ is the angle between the directions along which the optical depth is measured and the flow velocity.

3.2.2 Scattering and absorption

Next, we consider a photon transfer in a medium involving scattering and absorption process. The mean free path of a photon in the comoving frame is

$$l_0 = \frac{1}{\alpha_0 + \sigma_0}, \tag{3.10}$$

where α_0 and σ_0 are absorption and scattering coefficient in the comoving frame, respectively. The probability that a free path ends with a true absorption is

$$\epsilon = \frac{\alpha_0}{\alpha_0 + \sigma_0}. \tag{3.11}$$

If we assume that a photon is absorbed after N scatterings, the average number of scatterings N can be related to the ϵ by $N = 1/\epsilon$. Substituting this relation and equations (3.10) and (3.11) into equation (3.6), we obtain l_* as the functions of α_0 and σ_0:

$$l_*^2 = \left\{\frac{2}{3}\Gamma^2(\beta^2+3) + (\Gamma\beta)^2\frac{\sigma_0}{\alpha_0}\right\}\frac{1}{\alpha_0(\alpha_0+\sigma_0)}. \tag{3.12}$$

[4] This is also different from the one shown in the Rybicki & Lightman (1979), $N \simeq \xi^2 = \tau_0^2$ for the static medium, by the factor of 1/2 for the reason argued in Footnote 1.

Table 3.1. Approximate forms of effective optical depth τ_*

β	$\beta \ll \sqrt{2\tau_\mathrm{a}/\tau_\mathrm{s}}$	$\sqrt{2\tau_\mathrm{a}/\tau_\mathrm{s}} \ll \beta \ll 1$	$\beta \sim 1$
τ_*	$\sqrt{\tau_\mathrm{a}\tau_\mathrm{s}/2}$	τ_a/β	$2\tau_\mathrm{a}$

Note. — The top and bottom lines represent the ranges of the velocity β and approximated forms of effective optical depth τ_* in the ranges of β, respectively.

Introducing the optical depth for absorption and scattering in the observer frame as $\tau_\mathrm{a} = \Gamma(1-\beta\cos\Theta)\alpha_0 L$ and $\tau_\mathrm{s} = \Gamma(1-\beta\cos\Theta)\sigma_0 L$, respectively, the effective optical depth $\tau_* \equiv L/l_*$ becomes

$$\tau_* = \left\{\frac{2}{3}\Gamma^2(\beta^2+3) + (\Gamma\beta)^2\frac{\tau_\mathrm{s}}{\tau_\mathrm{a}}\right\}^{-1/2} \frac{\sqrt{\tau_\mathrm{a}(\tau_\mathrm{a}+\tau_\mathrm{s})}}{\Gamma(1-\beta\cos\Theta)}. \tag{3.13}$$

In the non-relativistic limit, equation (3.13) reduces to $\tau_* = \sqrt{\tau_\mathrm{a}(\tau_\mathrm{a}+\tau_\mathrm{s})/2}$, which is consistent with the effective optical depth in the static medium shown in Rybicki & Lightman (1979) except for the factor of $1/\sqrt{2}$ (see Footnotes 1 and 4).

Here, we consider scattering dominant case, i.e., $\tau_\mathrm{s} \gg \tau_\mathrm{a}$, which is the case in the GRB jets and cocoon. In this case, the behavior of τ_* depends on the relation between β and $\tau_\mathrm{a}/\tau_\mathrm{s}$. If $\beta \ll \sqrt{2\tau_\mathrm{a}/\tau_\mathrm{s}}$ ($\ll 1$), τ_* becomes $\tau_* \simeq \sqrt{\tau_\mathrm{a}\tau_\mathrm{s}/2}$. On the other hand, if $\beta \gg \sqrt{2\tau_\mathrm{a}/\tau_\mathrm{s}}$, τ_* is approximated by

$$\tau_* \simeq \frac{\tau_\mathrm{a}}{\Gamma^2\beta(1-\beta\cos\Theta)}. \tag{3.14}$$

If we calculate the optical depth along the velocity direction, i.e., $\Theta = 0$,

$$\tau_* \simeq \frac{1+\beta}{\beta}\tau_\mathrm{a}. \tag{3.15}$$

This can be approximated as

$$\tau_* \simeq \frac{\tau_\mathrm{a}}{\beta} \gg \tau_\mathrm{a}, \tag{3.16}$$

for the non-relativistic flow and

$$\tau_* \simeq 2\tau_{\rm a}, \tag{3.17}$$

for the relativistic flow. Therefore, the dependence of τ_* on $\tau_{\rm a}$ is different for $\beta \ll \sqrt{2\tau_{\rm a}/\tau_{\rm s}}$ and $\beta \gg \sqrt{2\tau_{\rm a}/\tau_{\rm s}}$. The effective optical depth τ_* is proportional to $\tau_{\rm a}$ when $\beta \gg \sqrt{2\tau_{\rm a}/\tau_{\rm s}}$ for the same reason that the number of scatterings is proportional to ξ when $\beta/\Gamma \gg \xi^{-1}$ in the pure scattering case as argued in Section 3.2.1. We summarize these approximated forms of τ_* for various ranges of β in Table 3.1.

The effective optical depth defines the photon production site as $\tau_* = 1$. From Equation (3.16), τ_* is much larger than $\tau_{\rm a} = 1$ as long as $\beta \ll 1$ even for $\beta \gg \sqrt{2\tau_{\rm a}/\tau_{\rm s}}$. This indicates that the photon production site in the flow with $\beta \ll 1$ is located at much outer region than the surface of $\tau_{\rm a} = 1$ as illustrated at the left of Figure 3.1. On the other hand, when the flow has relativistic velocity, τ_* differs from $\tau_{\rm a}$ by only the factor of 2 and the photon production site is located close to the surface of $\tau_{\rm a} = 1$ as illustrated at the right of Figure 3.1.

It should be noted that, even if the flow is non-relativistic, τ_* departures from the one for the static medium as long as the conditions of $\tau_{\rm s} \gg \tau_{\rm a}$ and $\beta \gg \sqrt{2\tau_{\rm a}/\tau_{\rm s}}$ are satisfied. This is because that a large number of scatterings makes the effect apparent even if the relativistic beaming has only a small effect at each scattering.

3.2.3 Comparisons with Numerical Simulations

In order to confirm the analytic arguments in Section 3.2, we perform radiative transfer simulations with the Monte Carlo method for the photons scattered in the relativistic flow. The simulations are performed with a Monte-Carlo radiative tranfer code described in Section 2.1. We compare the mean number of scatterings $\langle N \rangle$ with Equation (3.8).

We consider a uniform flow with a velocity β and the electron number density $n_{\rm e}$ of $10^{-10}/\sigma_{\rm T}$ cm^{-3}, where $\sigma_{\rm T}$ is Thomson scattering cross section. The flow velocity is parallel to z direction. Photons are created at the origin of the coordinate with an energy of $E_{\rm ph} = 0.1$ eV, which is set as to avoid the Klein-Nishina effect, in the comoving frame. We calculate the mean number of scatterings $\langle N \rangle$ while the photons travel a net distance L which ranges from 10^{11} to 10^{14} cm in the observer frame, so that the corresponding $\xi = n_{\rm e}\sigma_{\rm T}L$ ranges from 10 to 10^4. p Since our interests in this thesis is the influence of the fluid bulk motion on the number of scatterings,

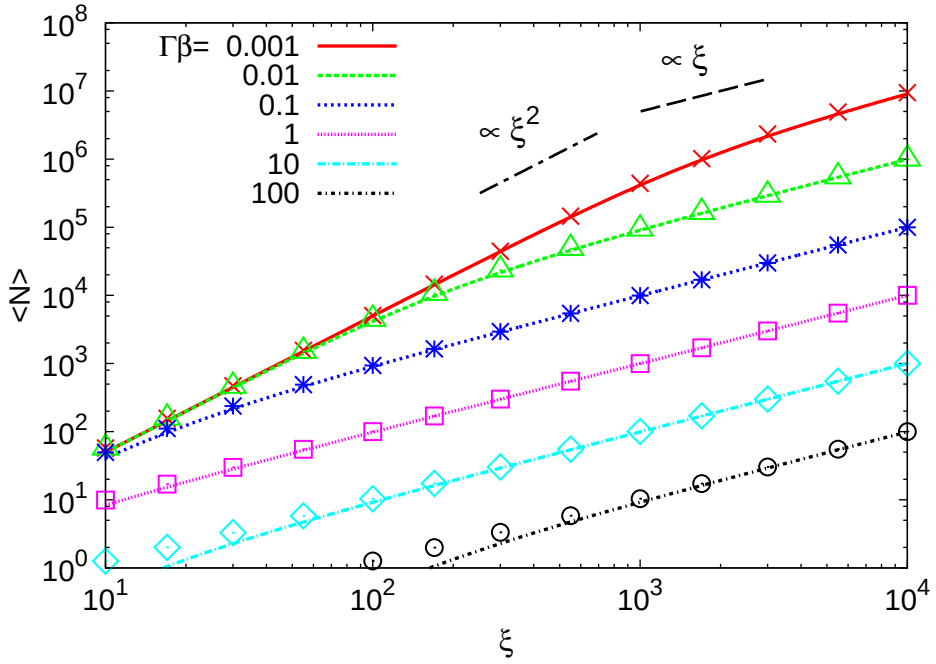

Figure 3.2 The mean number of scatterings $\langle N \rangle$ for the models with $\Gamma\beta = 10^{-3}$ (crosses), 10^{-2} (triangles), 10^{-1} (asterisks), 1 (squares), 10 (diamonds), and 100 (circles). The lines show the analytic expressions, equation (3.8), for the models denoted in the figure.

the temperature of the medium is set to be very low, i.e., $kT = 1\mathrm{eV}$, to avoid that the thermal motion of electrons affect the number of scatterings. We investigate non-relativistic and relativistic velocity of the medium with products of the Lorentz factor and the velocity $\Gamma\beta$ of 10^{-3}, 10^{-2}, 10^{-1}, 1, 10, and 10^2.

Figure 3.2 shows the mean number of scatterings $\langle N \rangle$ of 6×10^3 photons for the models with $\Gamma\beta = 10^{-3}$, 10^{-2}, 10^{-1}, 1 and 6×10^4 photons for the models with $\Gamma\beta = 10$ and 100. The lines show the analytic expressions derived in the previous section with $\Gamma\beta = 10^{-3}, 10^{-2}, 10^{-1}, 1, 10$ and 100 (Eq. (3.8)). This demonstrates that the analytic expressions are excellently consistent with the results of numerical simulations, except at $\langle N \rangle \sim 1$. The difference at the region comes from the fact that a considerable number of photons do not experience any scatterings in this region, although the equation (3.8) is obtained assuming all the photons undergo more than one scatterings.

The dependencies of $\langle N \rangle$ on ξ are as follows: In the model with $\Gamma\beta = 10^{-3}$, $\langle N \rangle$

is proportional to ξ^2 for $\xi < 10^3 \simeq \beta^{-1}$ and to ξ for $\xi > 10^3$. In the model with $\Gamma\beta = 10^{-2}$, $\langle N \rangle$ is proportional to ξ^2 for $\xi < 10^2$ and to ξ for $\xi > 10^2$. The transition of the dependence is at $\xi \sim \beta^{-1}$. In the models with $\Gamma\beta = 10^{-1}$, 1, and 10, $\langle N \rangle$ is proportional to ξ in the range of $10 < \xi < 10^4$. In the model with $\Gamma\beta = 100$, $\langle N \rangle$ is proportional to ξ for $\xi > 10^2$.

3.3 Summary

In this chapter, we investigate the random walk process in relativistic flow. In the pure scattering medium, the mean number of scatterings at the size parameter of ξ is proportional to ξ^2 for $\beta/\Gamma \ll \xi^{-1}$ and to ξ for $\beta/\Gamma \gg \xi^{-1}$. These dependencies of the mean number of scatterings on ξ are well reproduced by the numerical simulations. We also consider the combined scattering and absorption case. If the scattering opacity dominates the absorption opacity, the behavior of the effective optical depth is different depending on the velocity β. If $\beta \ll \sqrt{2\tau_{\rm a}/\tau_{\rm s}}$, the effective optical depth is $\tau_* \simeq \sqrt{\tau_{\rm a}\tau_{\rm s}/2}$ and if $\beta \gg \sqrt{2\tau_{\rm a}/\tau_{\rm s}}$, $\tau_* \simeq (1+\beta)\tau_{\rm a}/\beta$.

In GRB jets, the flow has a ultra-relativistic velocity ($\Gamma \gtrsim 100$) and the electron scattering opacity dominates the absorption opacity ($\tau_{\rm s} \gg \tau_{\rm a}$) due to its low density and high temperature. Thus, the effective optical depth in the jet is approximated by $\tau_* \simeq 2\tau_{\rm a}$. On the other hand, the cocoon have a non-relativistic velocity (e.g., Matzner 2003) and the effective optical depth in the cocoon could be much higher than the absorption optical depth as $\tau_* \simeq \tau_{\rm a}/\beta \gg \tau_{\rm a}$. The effective optical depth defines the photon production site as $\tau_* = 1$. In the subsequent papers, we will perform the radiative transfer calculations for the thermal radiation from GRB jet and cocoon taking into account the photon production at the surface of $\tau_* = 1$. This enables us to correctly treat the photon number density at the photon production sites.

The results could be applicable not only for GRB jet and cocoon but also for the other astronomical objects such as AGNs or black hole binaries. For example, the super critical accretion flows around the black holes produce a high temperature ($\sim 10^8$ K) and low density ($\sim 10^{-9}$ g/cm^3) outflow with a semi-relativistic velocity ($\sim 0.1c$) (e.g., Kawashima et al. 2009). In these circumstances, the scattering process have a major role on the photon diffusion and the relativistically corrected treatment is necessary even though the flow velocity is rather small compared with the speed of

light.

CHAPTER 4
THERMAL RADIATION FROM GAMMA-RAY BURST JET

4.1 Overview

As described in Section 1.3, the radiation mechanism of GRB prompt emission is under debate. Although the internal shock model had been thought to be a standard scenario for the prompt emission, it is known that the model has problems about radiative efficiency and the low energy power law spectral index (e.g., Preece et al. 1998). Thus, the alternative models are required at least for the burst which cannot be explained by the internal shock model.

One of such alternative models is the thermal emission model which explains the prompt emission with the thermal emission from relativistic jets. The thermal emission from GRB outflow is a natural consequence of the relativistic fireball model and has been investigated by many authors since the first suggestions of the fireball model by Goodman (1986) and Paczynski (1986).

Thermal radiation from GRB jets have been investigated by many authors. For example, Lazzati et al. (2009, 2011); Mizuta et al. (2011); Nagakura et al. (2011) calculated the light curves or energy spectra by superposing blackbody radiation emitted from the photosphere, i.e. from the surface of $\tau = 1$ where τ is the optical depth. However, since the dominant opacity source in the GRB jet is the electron scattering, the photosphere is just a surface around which the observed photons experience their last scatterings before escaping from the jet and the radiaion and absorption processes are extremely inefficient around the photosphere. This implies that the observed photons should be generated far below the photosphere (Beloborodov 2013), propagate through the jet with experiencing many scatterings, and escape from the jet. Therefore, in order to treat the thermal radiation from GRB jets properly, both the radiative transfer in the jets and complex structures of the jets should be taken into account.

In this chapter, we perform radiative transfer simulation with complicated inner structures of the jet calculated by performing a hydrodynamical simulation. Then, we present the results of hydrodynamical simulation and radiative transfer simulation.

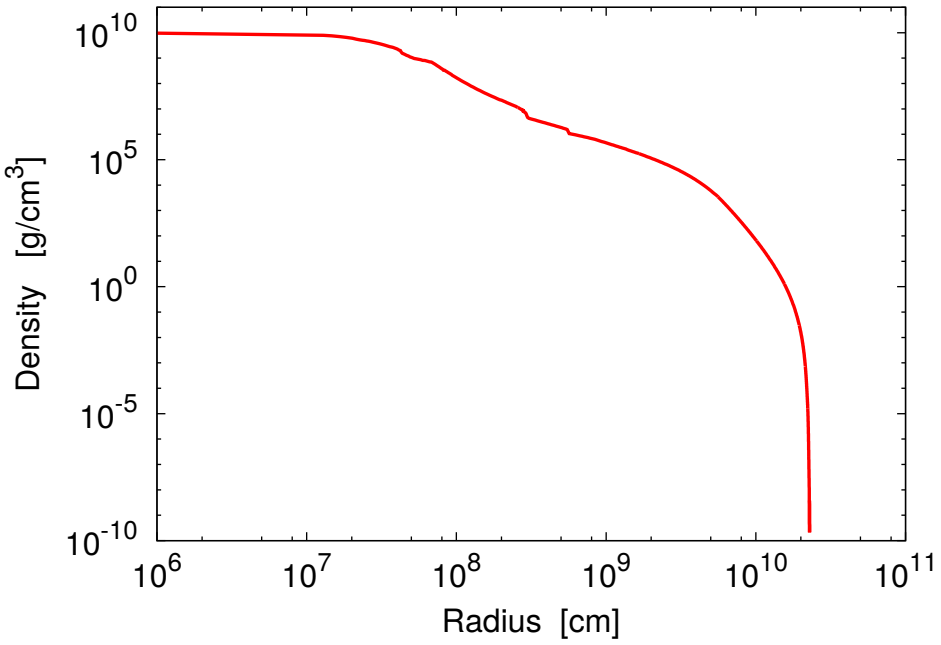

Figure 4.1 The density structure of the progenitor star whose mass and metallicity are $15M_\odot$ and $Z = 10^{-3}$, respectively.

4.2 Method

4.2.1 Hydrodynamical Simulation

The jet structure is calculated by 2D relativistic hydrodynamics code with newtonian self gravity (Section 2.2). A $15M_\odot$ Wolf-Rayet star with the metallicity of $Z = 10^{-3}$ is used for the progenitor star (Umeda & Nomoto 2005; Nomoto et al. 2006) whose density structure is shown in Figure 4.1. The radius of the star is $\sim 2.3 \times 10^{10}$ cm.

The inner boundary is set to be $r_{\rm in} = 10^9$ cm and the computational domain is captured by 600 logalithmical grids in the r-direction and 150 uniform grids in the θ-direction. The outer boundary of the domain is initially at 2.5×10^{10} cm and elongated twice when the shock wave reaches near the boundary.

The relativistic jet is injected by imposing boundary conditions at $r_{\rm in}$. The conditions are the total jet luminosity $L_{\rm jet} = 5.3 \times 10^{50}$ erg s^{-1}, the initial Lorentz factor $\Gamma_0 = 5$, the half opening angle of the jet $\theta_0 = 10°$, and the thermal to total energy density ratio $f_{\rm th} = 0.9925$ which corresponds to the conditions of specific internal energy $\varepsilon_0/c^2 = 80$.

4.2.2 Photon Production Site

We evaluate the effective optical depth τ_* to determine where the observed photons are produced. With the expression for τ_* in relativistic flow derived in Shibata et al. (2014), τ_* from infinity to a radius R_* can be calculated as

$$\tau_* = \int_{R_*}^{\infty} \left\{ \frac{\Gamma^2}{3}(\beta^2+3) + (\Gamma\beta)^2 \frac{\sigma'}{\alpha'} \right\}^{-\frac{1}{2}} \sqrt{\alpha'(\alpha'+\sigma')} dr, \tag{4.1}$$

where σ' and α' are the scattering and the absorption coefficient in the fluid comoving frame, respectively. The scattering coefficient is calculated with the Thomson scattering cross secion as $\sigma' = n_{\rm e}\sigma_{\rm T}$. The absorption coefficient include two processes. One is the free-free absorption (e.g., Rybicki & Lightman 1979) and the other is the double Compton absorption (e.g., Lightman 1981; Svensson 1984; Beloborodov 2013; Vurm et al. 2013). Then absorption coefficient for the photon with the energy $x \equiv h\nu/m_{\rm e}c^2$ can be written as

$$\alpha'(x) = \alpha'_{\rm ff}(x) + \alpha'_{\rm DC}(x), \tag{4.2}$$

where $\alpha'_{\rm ff}(x)$ and $\alpha'_{\rm DC}(x)$ are the absorption coefficient for the free-free and the double Compton absorption, respectively.

The absorption coefficient of the free-free absorption is written as (e.g., Rybicki & Lightman 1979)

$$\alpha'_{\rm ff}(x) = \frac{\alpha_{\rm fin}\lambda_{\rm c}^3\sigma_{\rm T}}{\sqrt{6}\pi}\Theta^{-\frac{1}{2}}Z^2 n_{\rm e} n_{\rm i} x^{-3}(1-e^{-x/\Theta}) g_{\rm ff}, \tag{4.3}$$

where $\alpha_{\rm fin}$ is the fine structure constant, $\lambda_{\rm c}$ is the Compton wavelength, $\Theta = kT/m_{\rm e}c^2$ is the temperature in units of the electron rest mass energy, Z is the atomic number of the ion, $n_{\rm e}$ is the electron number density, $n_{\rm i}$ is the ion number density, and $g_{\rm ff}$ is the frequency averaged Gaunt factor. We assume that the ions consist of helium, which means $Z = 2$ and $n_{\rm i} = n_{\rm e}/2$.

The absorption coefficient of the double Compton absorption for Wien distribution is written as (e.g., Svensson 1984)

$$\alpha'_{\rm DC}(x) = \frac{2\alpha_{\rm fin}\lambda_{\rm c}^3\sigma_{\rm T}}{\pi^2}\Theta^{\frac{1}{2}} n_{\rm e} n_\gamma x^{-3}(e^{x/\Theta}-1) g_{\rm DC}, \tag{4.4}$$

where n_γ is the photon number density and $g_{\rm DC}$ is a numerical fitting factor which

can be expressed as

$$g_{\rm DC} = (1 + 13.91\Theta + 11.05\Theta^2 + 19.92\Theta^3)^{-1}. \tag{4.5}$$

In order to calculate $\alpha'_{\rm DC}(x)$, we have to know the number density of background photons n_γ at any radius. Although the exact value of n_γ can be obtained by performing many radiative transfer calculations iteratively, such iterations must involve large computational costs. Therefore, we assume that the photons are produced at a radius R_* with the number density of the blackbody photons

$$n_{\gamma *} \equiv n_\gamma(R_*) = 8\pi\Gamma(3)\zeta(3)\left(\frac{kT}{hc}\right)^3, \tag{4.6}$$

where $\Gamma(3)\zeta(3) \simeq 2.404$, and $n_\gamma(r)$ decreases as

$$n_\gamma(r) = n_{\gamma *}\left(\frac{R_*}{r}\right)^2. \tag{4.7}$$

To eliminate dependence of the frequency in Eq. (4.3) and (4.4), we assume that the energy of the photon for which the effective optical depth is calculated is equal to kT, i.e. $x = \Theta$, because the equipartition between photon energy density and thermal energy density of the plasma take place at $\tau \gg 1$ due to a lot of electron scatterings.

We find $R_* = R_{*1}$ which satisfies $\tau_* = 1$ for each zenith angle θ from jet axis and obtain the surface at which we assume that the observed photons are produced.

4.2.3 Radiative Transfer Simulation

Radiative transfer simulations are performed with the numerical code based on Monte Carlo method. We calculate the change of the energy and the propagation direction of the photons with random numbers. In the calculations, both the fluid bulk motion and the thermal motion of the electrons are included with special relativistic treatments. The Klein-Nishina cross section is used for the scattering cross section. The details of the numerical code are described in Section 2.1.

For simplicity, we take a snapshot of the result of hydrodynamical simulation at $t = 40$ s as the hydrodynamical background of the radiative transfer simulations.

Photons are injected at the surface of $\tau_* = 1$. The energies of injected photons

are initially determined as to obey the Planck distribution with its local plasma temperatures. The propagation directions of the injected photons are isotropic in the fluid rest frame. The spatial distribution of the injected photons at the surface is determined by the temperature distribution at the surface since we assume that the photons are injected as the blackbody radiation whose photon number density is proportional to cubic of the temperature, $n \propto T^3$.

After the injection, the photons propagate through the jet with a lot of scatterings by electrons and escape from the jet when the scattering optical depth decreases to one or so. We collect the photons escaped parallel to the jet axis and construct the energy spectrum. The number of injected photons is 3×10^8.

4.3 Results

4.3.1 Structures of the Jet and the Cocoon

Figure 4.2 shows the density structure of the jet and the cocoon derived by the hydrodynamical simulation. We also show the surface of $\tau_* = 1$. Near the jet axis, the density is quite low and the free-free absorption is correspondingly very inefficient since absorption coefficient of the free-free absorption is proportional to the square of the electron number density, $n_{\rm e}^2$ (see Eq. 4.3), although the absorption coefficient of the double Compton absorption is proportional to $n_{\rm e}$. Thus, the main absorption process is the double Compton absorption in the jet. On the other hand, the density in the cocoon is much higher than that in the jet. Such high density makes free-free absorption be the main absorption process in the cocoon and the surface of $\tau_* = 1$ locates at much larger radius in the cocoon.

The difference of the dominant absorption process causes sudden transition of the location of $\tau_* = 1$ surface. The transition occurs at $\theta_{\rm tr} \simeq 6.1^\circ$. This angle is smaller than the half opening angle which is imposed as the inner boundary condition in the hydrodynamical simulation, $\theta_0 = 10^\circ$, since the shape of the jet is collimated due to the interaction of the jet and the stellar matter even after the jet breaks out the stellar surface.

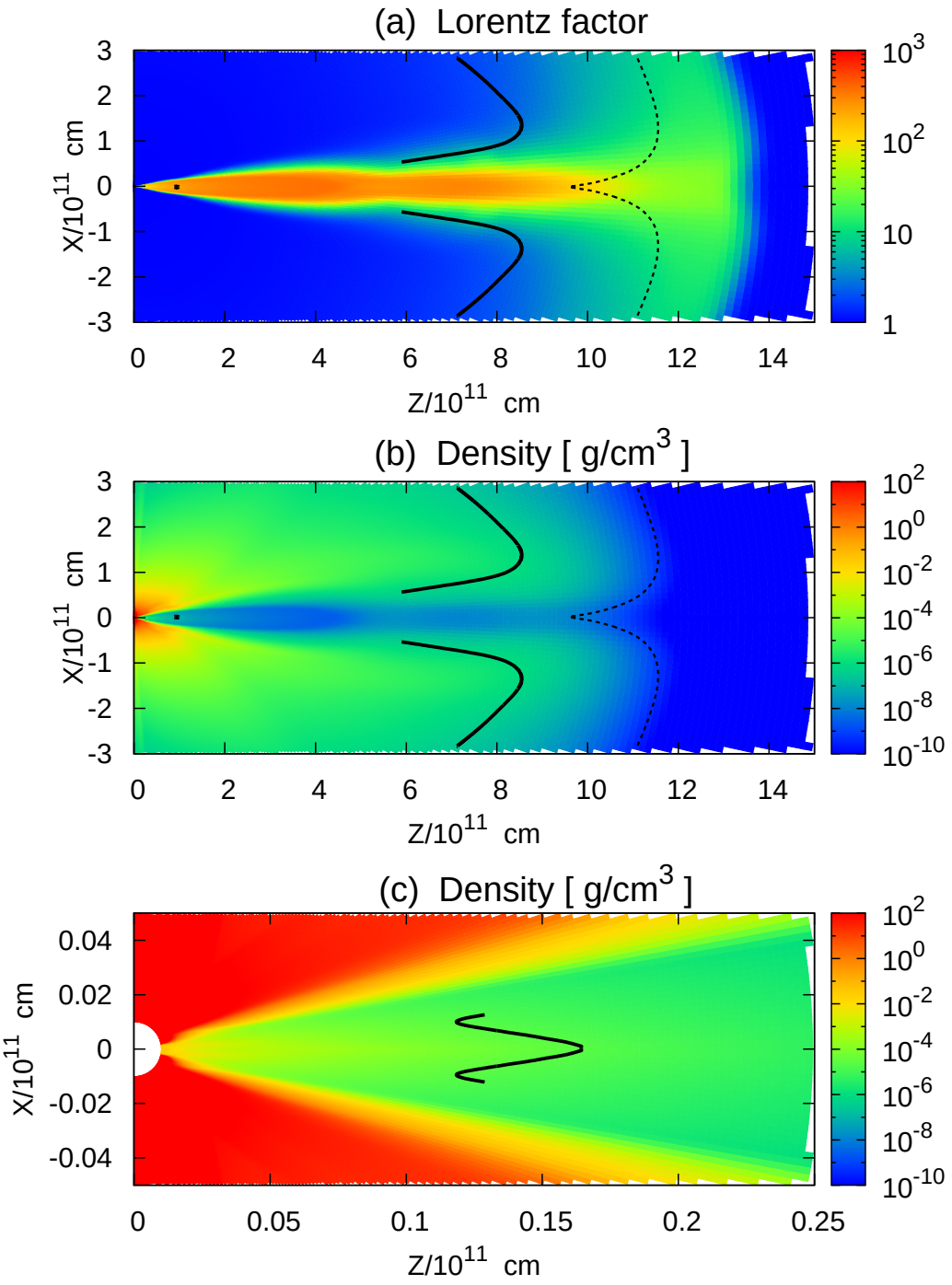

Figure 4.2 The density structure of the jet. The upper and lower panels show the overall structure and the base of the jet, respectively. The solid line represents the surface of $\tau_* = 1$. We also show the photosphere by the dotted line for comparison.

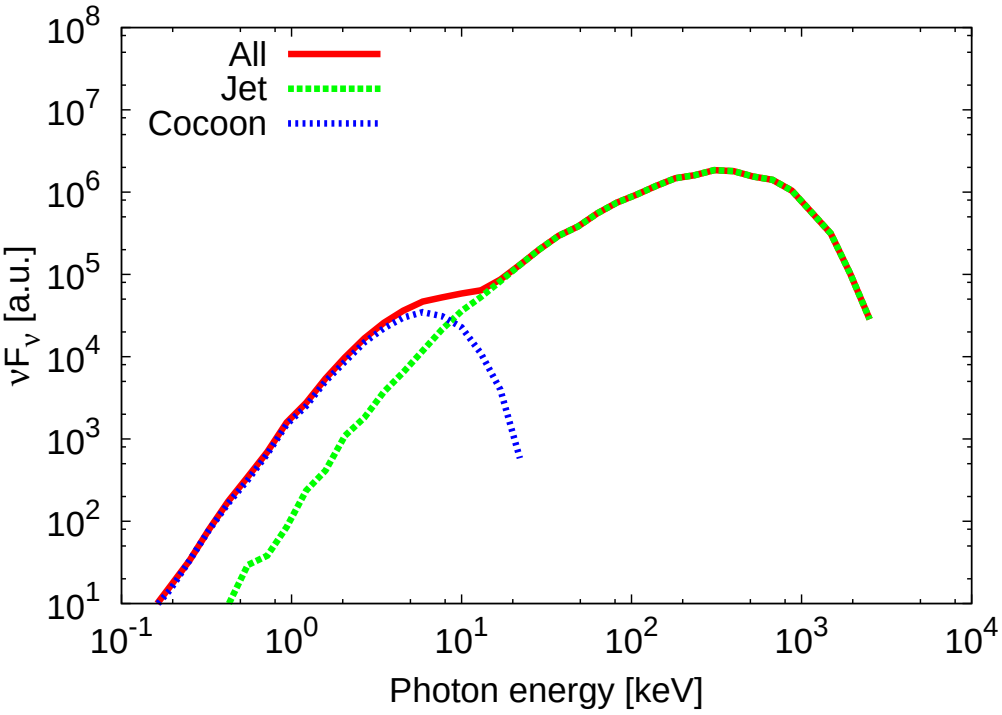

Figure 4.3 The observed spectrum. The red solid represents the entire spectrum. The green dashed and the blue dotted lines represent the contributions from the jet and the cocoon, respectively.

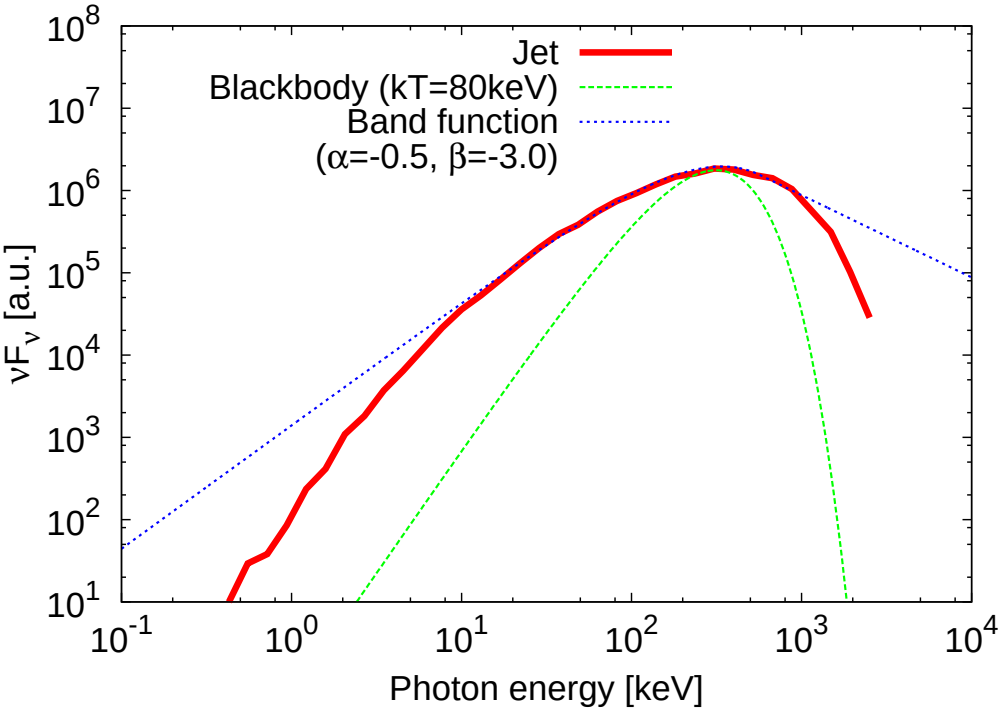

Figure 4.4 The observed spectrum. The dotted line represents the Band function with low and high energy photon indexes of $\alpha = -0.5$ and $\beta = -3$.

4.3.2 Observed Spectrum

Figure 4.3 shows the energy spectrum observed along the jet axis. Here we divide the spectrum into two components. Contributions from photons which were injected at $\theta \leq \theta_{\rm tr}$ are labeled as jet component and photons injected at $\theta > \theta_{\rm tr}$ are labeled as cocoon component. The observed spectrum mainly consist of the jet component, although the cocoon component contributes to the spectrum at much lower energies. The difference of the peak energies between two components is due to the difference of typical Lorentz factors of the components around the photosphere (Fig. 4.2(a)) and the difference of the directions of velocity field because the degree of Doppler boost of photons energies depends on both the Lorentz factor and the angle between the directions of the photon propagation and the velocity field. Higher degree of Doppler boost makes the observed energies of photons higher.

The energy spectrum of the jet component has a peak energy of $E_{\rm p} \simeq 300$ keV. Figure 4.4 shows the comparison between the our result and a pure blackbody spec-

trum with the temperature of $kT = 80$ keV. From the figure, it can be seen that the emergent spectrum has much wider shape than the pure blackbody.

Figure 4.4 also shows a Band function with low and high energy photon indexes of $\alpha = -0.5$ and $\beta = -3$, respectively. These parameters are consistent with the observed spectra (Figure 1.7), although they are not typical value. The emergent spectrum can be well fitted by the Band function if we focus only on the energy range between 10 keV and 1 MeV. However, the spectrum has a cutoff above 1 MeV and conflict with the fact that there are many bursts which have high energy power law even beyond 10 times the peak energy.

4.4 Summary & Discussions

In this chapter, we investigate the spectrum of thermal radiation from relativistic GRB jet. We calculate radiative transfer for thermal photons in a relativistic GRB jet of which structure is derived with 2D special relativistic hydrodynamic simulation. The radiative transfer is calculated with a numerical code based on Monte-Carlo method.

We find that the radiation from a sub-relativistic cocoon partially contributes to the spectrum at lower energies, although the spectrum mainly consist of the radiation from ultra-relativistic jet. We compare our results to the Band function and find that the spectrum can be well fitted by the Band function around the peak energy, indicating that thermal emission may be observed as a non-thermal Band function.

The emergent spectrum mainly consists of the jet component and the cocoon component contributes to the spectrum at much lower energies. Since we performed radiative transfer calculation with a snapshot of the jet structure, the spectrum is a superposition of these two components. However, it is expected that the photons escaping through the cocoon take longer paths than the photons escaping through the jet. This implies that the cocoon component could be observed at much later epoch than the jet component (e.g., Lundman et al. 2013). In fact, some authors have suggested that the thermal emission from the cocoon could be observed at early afterglow phase (e.g., Pe'er et al. 2006; Suzuki & Shigeyama 2013).

We found that the emergent spectrum is much wider than a pure blackbody spectrum. On the other hand, the spectrum can be well fitted by the Band function with parameters that is consistent with the observations if we focus only on the energy

range between 10keV and 1MeV although the spectrum has no power law component beyond 1MeV. Rencently, there are some claims that thermal components are exist on the non-thermal Band functions for several burst (e.g., Guiriec et al. 2011; Axelsson et al. 2012). In these claims, thermal components are treated as a single temperature blacbody spectrum. However, according to our result, the shape of the thermal components may be different from that of the pure blackbody radiation. Thus, we need to be carefull for the treatment of thermal components.

We used a snapshot of the result of hydrodynamical simulation for the jet structure. However, relativistic jets have velocities which are similar to speed of light and the fluid motion during the photon propagation could be important for radiative transfer calculations. For example, the fluid bulk motion can affect the estimation of the optical depth(Nagakura et al. 2011) and change the position of the photosphere and photon production site. Furthermore, shock waves propagating with comparable speed of light are known as the site which energize the photons propagating many times through the shock (Blandford & Payne 1981). In fact, it is suggested that the energization of photons by shock waves is important for the formation of non-thermal spectrum of the radiation from relativisitc shock breakout (e.g., Wang et al. 2007; Suzuki & Shigeyama 2010). In order to include the fluid motion during the photon propagation, we will perform time dependent radiative transfer simulation in future. Such time dependent calculations can provide consistent light curves and spectral evolution which should be important information.

We investigate only for one model in this thesis. The spectrum should depends on the jet parameters such as luminosity, opening angle, or total energy. The property of the progenitor and circum stellar matter may also be important. The dimensionality of the hydrodynamical simulation should also affect the radiative properties. In 3-dimensional simulations, the structure of relativistic jet could be more complex than the result of 2-dimensional simulation (e.g., López-Cámara et al. 2013). For example, Rayleigh-Taylor instability on the boundary between the jet and the stellar matter may be important for the dynamics of the jet and make the jet more complex (Matsumoto & Masada 2013). Such complexity of the jet could lead to the diversity of propagating photons and affect the observational properties.

CHAPTER 5
SUMMARY

In this thesis, we investigate the random walk process in relativistic flow and construct an analytic expression for the effective optical depth in relativistic flow. Then, we apply the theory to the thermal photons radiated from relativistic jet which penetrates from massive star and results in the gamma-ray burst.

We investigate the random walk process in the relativistic flow. In the pure scattering medium, the mean number of scatterings at the size parameter of ξ is proportional to ξ^2 for $\beta/\Gamma \ll \xi^{-1}$ and to ξ for $\beta/\Gamma \gg \xi^{-1}$. These dependencies of the mean number of scatterings on ξ are well reproduced by the numerical simulations. We also consider the combined scattering and absorption case. If the scattering opacity dominates the absorption opacity, the behavior of the effective optical depth is different depending on the velocity β. If $\beta \ll \sqrt{2\tau_{\rm a}/\tau_{\rm s}}$, the effective optical depth is $\tau_* \simeq \sqrt{\tau_{\rm a}\tau_{\rm s}/2}$ and if $\beta \gg \sqrt{2\tau_{\rm a}/\tau_{\rm s}}$, $\tau_* \simeq (1+\beta)\tau_{\rm a}/\beta$.

Applying the derived analytic expression for the effective optical depth, we investigate the spectrum of thermal radiation from relativistic GRB jet. We calculate radiative transfer for thermal photons in a relativistic GRB jet of which structure is derived with 2D special relativistic hydrodynamic simulation. The radiative transfer is calculated with a numerical code based on Monte-Carlo method. We found that the emergent spectrum has a much wider shape than a pure blackbody spectrum. On the other hand, the spectrum can be well fitted by the Band function with parameters that is observationally consistent with the observations if we focus on the energy range between 10keV and 1MeV, while the spectrum has no power laws beyond 1MeV, indicating that the thermal emission may be observed as a non-thermal Band function.

There are some claims that the thermal components exist on the non-thermal Band functions for several bursts (e.g., Guiriec et al. 2011; Axelsson et al. 2012). In these claims, thermal components are treated as a single temperature blacbody spectrum. However, according to our result, the shape of the thermal components may be different from that of the pure blackbody radiation. Thus, we need to be carefull for the treatment of thermal components.

ACKNOWLEDGEMENT

The author would like to express his deep and sincere gratitude to Prof. Nozomu Tominaga for his a lot of valuable advices throughout this work. The author wishes to thank Prof. Hajime Susa and Dr. Masaomi Tanaka for their fruitful comments and discussions on this work. The author also would like to thank Dr. Akihiro Suzuki for his helpful advices for the construction of the Monte-Carlo radiative transfer code.

REFERENCES

Abramowicz, M. A., Novikov, I. D., & Paczynski, B. 1991, ApJ, 369, 175

Axelsson, M., Baldini, L., Barbiellini, G., et al. 2012, ApJ, 757, L31

Band, D., Matteson, J., Ford, L., et al. 1993, ApJ, 413, 281

Beloborodov, A. M. 2010, MNRAS, 407, 1033

—. 2013, ApJ, 764, 157

Blandford, R., & Eichler, D. 1987, Phys. Rep., 154, 1

Blandford, R. D., & McKee, C. F. 1976, Physics of Fluids, 19, 1130

Blandford, R. D., & Payne, D. G. 1981, MNRAS, 194, 1033

Briggs, M. S., Band, D. L., Kippen, R. M., et al. 1999, ApJ, 524, 82

Bykov, A. M., & Meszaros, P. 1996, ApJ, 461, L37

Costa, E., Frontera, F., Heise, J., et al. 1997, Nature, 387, 783

Djorgovski, S. G., Kulkarni, S. R., Bloom, J. S., et al. 1998, ApJ, 508, L17

Donat, R., Font, J. A., Ibáñez, J. M., & Marquina, A. 1998, Journal of Computational Physics, 146, 58

Fishman, G. J., & Meegan, C. A. 1995, ARA&A, 33, 415

Fox, D. B., Frail, D. A., Price, P. A., et al. 2005, Nature, 437, 845

Freiburghaus, C., Rembges, J.-F., Rauscher, T., et al. 1999, ApJ, 516, 381

Galama, T. J., Vreeswijk, P. M., van Paradijs, J., et al. 1998, Nature, 395, 670

Giannios, D. 2006, A&A, 457, 763

—. 2008, A&A, 480, 305

—. 2012, MNRAS, 422, 3092

Goodman, J. 1986, ApJ, 308, L47

Guiriec, S., Connaughton, V., Briggs, M. S., et al. 2011, ApJ, 727, L33

Hachisu, I. 1986, ApJS, 62, 461

Harrison, F. A., Bloom, J. S., Frail, D. A., et al. 1999, ApJ, 523, L121

Hjorth, J., Sollerman, J., Møller, P., et al. 2003, Nature, 423, 847

Ito, H., Nagataki, S., Ono, M., et al. 2013, ApJ, 777, 62

Iwamoto, K., Mazzali, P. A., Nomoto, K., et al. 1998, Nature, 395, 672

Johnson, M. H., & McKee, C. F. 1971, Phys. Rev. D, 3, 858

Kaneko, Y., Preece, R. D., Briggs, M. S., et al. 2006, ApJS, 166, 298

Katz, J. I. 1994, ApJ, 432, L107

—. 1997, ApJ, 490, 633

Kawashima, T., Ohsuga, K., Mineshige, S., et al. 2009, PASJ, 61, 769

Klebesadel, R. W., Strong, I. B., & Olson, R. A. 1973, ApJ, 182, L85

Kobayashi, S., Piran, T., & Sari, R. 1997, ApJ, 490, 92

Kulkarni, S. R., Djorgovski, S. G., Ramaprakash, A. N., et al. 1998, Nature, 393, 35

Lazzati, D., Morsony, B. J., & Begelman, M. C. 2009, ApJ, 700, L47

—. 2011, ApJ, 732, 34

Lightman, A. P. 1981, ApJ, 244, 392

Lithwick, Y., & Sari, R. 2001, ApJ, 555, 540

López-Cámara, D., Morsony, B. J., Begelman, M. C., & Lazzati, D. 2013, ApJ, 767, 19

Lundman, C., Pe'er, A., & Ryde, F. 2013, MNRAS, 428, 2430

Marquina, A., Marti, J. M., Ibanez, J. M., Miralles, J. A., & Donat, R. 1992, A&A, 258, 566

Marti, J. M., & Muller, E. 1994, Journal of Fluid Mechanics, 258, 317

Martí, J. M., & Müller, E. 1996, Journal of Computational Physics, 123, 1

Matsumoto, J., & Masada, Y. 2013, ApJ, 772, L1

Matzner, C. D. 2003, MNRAS, 345, 575

McKee, C. R., & Colgate, S. A. 1973, ApJ, 181, 903

Mészáros, P. 2006, Reports on Progress in Physics, 69, 2259

Meszaros, P., Laguna, P., & Rees, M. J. 1993, ApJ, 415, 181

Meszaros, P., & Rees, M. J. 1993, ApJ, 405, 278

Mészáros, P., & Rees, M. J. 2000, ApJ, 530, 292

Metzger, M. R., Djorgovski, S. G., Kulkarni, S. R., et al. 1997, Nature, 387, 878

Mizuta, A., Nagataki, S., & Aoi, J. 2011, ApJ, 732, 26

Nagakura, H., Ito, H., Kiuchi, K., & Yamada, S. 2011, ApJ, 731, 80

Nakauchi, D., Kashiyama, K., Suwa, Y., & Nakamura, T. 2013, ApJ, 778, 67

Nomoto, K., Tominaga, N., Umeda, H., Kobayashi, C., & Maeda, K. 2006, Nuclear Physics A, 777, 424

Paciesas, W. S., Meegan, C. A., Pendleton, G. N., et al. 1999, ApJS, 122, 465

Paczynski, B. 1986, ApJ, 308, L43

Pe'er, A., Mészáros, P., & Rees, M. J. 2006, ApJ, 652, 482

Piran, T. 2004, Reviews of Modern Physics, 76, 1143

Piran, T., Shemi, A., & Narayan, R. 1993, MNRAS, 263, 861

Preece, R. D., Briggs, M. S., Mallozzi, R. S., et al. 1998, ApJ, 506, L23

Racusin, J. L., Oates, S. R., Schady, P., et al. 2011, ApJ, 738, 138

Rees, M. J., & Meszaros, P. 1994, ApJ, 430, L93

Rees, M. J., & Mészáros, P. 2005, ApJ, 628, 847

Ruderman, M. 1975, in Annals of the New York Academy of Sciences, Vol. 262, Seventh Texas Symposium on Relativistic Astrophysics, ed. P. G. Bergman, E. J. Fenyves, & L. Motz, 164–180

Rybicki, G. B., & Lightman, A. P. 1979, Radiative processes in astrophysics

Ryde, F., Axelsson, M., Zhang, B. B., et al. 2010, ApJ, 709, L172

Sari, R., Narayan, R., & Piran, T. 1996, ApJ, 473, 204

Sari, R., Piran, T., & Narayan, R. 1998, ApJ, 497, L17

Shibata, S., Tominaga, N., & Tanaka, M. 2014, ApJ, 787, L4

Shu, C.-W., & Osher, S. 1988, Journal of Computational Physics, 77, 439

Sunyaev, R. A., & Titarchuk, L. G. 1980, A&A, 86, 121

Suzuki, A., & Shigeyama, T. 2010, ApJ, 719, 881

—. 2013, ApJ, 764, L12

Svensson, R. 1984, MNRAS, 209, 175

Tominaga, N. 2009, ApJ, 690, 526

Umeda, H., & Nomoto, K. 2005, ApJ, 619, 427

van Paradijs, J., Groot, P. J., Galama, T., et al. 1997, Nature, 386, 686

Vurm, I., Lyubarsky, Y., & Piran, T. 2013, ApJ, 764, 143

Wang, X.-Y., Li, Z., Waxman, E., & Mészáros, P. 2007, ApJ, 664, 1026

Zhang, B., Fan, Y. Z., Dyks, J., et al. 2006, ApJ, 642, 354